STATIC AND DYNAMIC COMPRESSIVE RESPONSE OF ADDITIVELY MANUFACTURED DISCRETE PATTERNS OF Ti6Al4V

D. Levy , A. Shirizly , D. Rittel

PII: S0734-743X(18)30212-4
DOI: 10.1016/j.ijimpeng.2018.07.014
Reference: IE 3139

To appear in: *International Journal of Impact Engineering*

Received date: 10 March 2018
Revised date: 21 July 2018
Accepted date: 23 July 2018

Please cite this article as: D. Levy , A. Shirizly , D. Rittel , STATIC AND DYNAMIC COMPRESSIVE RESPONSE OF ADDITIVELY MANUFACTURED DISCRETE PATTERNS OF Ti6Al4V , *International Journal of Impact Engineering* (2018), doi: 10.1016/j.ijimpeng.2018.07.014

Highlights

- Additively manufactured (AM) discrete patterns made of Ti6Al4V offer potential energy absorption for engineering applications.
- We compared 3 different patterns with a similar mass and cross-section.
- The static and dynamic mechanical responses of the columnar pattern differ.
- Failure mode of axisymmetric elastic-plastic collapse (Tube I) was found to be preferable for energy absorption.

STATIC AND DYNAMIC COMPRESSIVE RESPONSE OF ADDITIVELY MANUFACTURED DISCRETE PATTERNS OF Ti6Al4V

D. Levy[1,2*], A. Shirizly[1,2], D. Rittel[1]

[1] *Technion –Faculty of Mechanical Engineering, Technion, Haifa, 32000, Israel*

[2] *RAFAEL – P. O. B 2250, Haifa 3102102, Israel*

Abstract

Additively manufactured (AM) discrete patterns made of Ti6Al4V offer potential energy absorption for engineering applications, including blast and impact protection systems, aircraft structure, automotive, and medical applications. In this study, we compared three different cylindrical printed patterns fabricated by selective laser melting (SLM), patterns sharing similar cross section and mass, in order to identify the "optimal" design of such structures for energy absorption purposes. The specimens consist of one columnar and two tubular patterns. The columnar pattern (8-Column) was constructed out of uniformly distributed columns. The first tubular pattern (Tube I) was constructed with the same outer diameter and tapered inner profile. The second tubular pattern (Tube II) had adjusted internal and external diameters. Quasi-static and impact (dynamic) load tests were performed to investigate the strain rate dependency, compressive response and failure mode of each pattern, including a comparison with a printed solid reference cylinder. Numerical simulations were carried out to complement the experimental work and to develop a generic numerical tool for future structural optimization applications. The results show that the geometry has a strong influence on its overall compressive performance, including energy absorption. The most effective of the patterns investigated was Tube I for both quasi-static and dynamic regimes.

* Corresponding author: D. Levy, *daniel55@campus.technion.ac.il*

1. Introduction

The advantage offered by additive manufacturing's (AM) is the ability to manufacture complex shapes that cannot be produced using conventional manufacturing methods. As an example, this technology allows the manufacture of discrete patterns or lattice structures with high density and different orientations. Over the past two decades, research on AM has focused on bulk material under fatigue[1], voided solids[2], mechanical properties, building orientation[3,4], residual manufacture stress, selective laser melting (SLM) improvements[5] and thermal treatments for fracture toughness[6]. Recently, the potential lattice structures have for lightweight energy absorbing structures has attracted renewed interest. This is the direct result of AM technology and finite element (FE) models used to predict the compressive response[7]. Those models have proven to predict accurate results, and therefore greatly reduce the amount of laboratory work and lower costs. The Ti6Al4V alloy has been widely covered for AM purposes according to the ASTM F2924-14 standard[8]. It is suitable to engineering structures requiring a combination of low weight, high strength, and elevated temperatures (up to 400^0C). To those characteristics, one must add high durability and excellent corrosion resistance, which means that Ti6Al4V is extensively used in aerospace, automotive and medical applications.

Complex shapes such as cellular solids or lattice structures can be manufactured quickly and easily using SLM methods. Inner content can be designed, orientated and built specifically[9–11] to meet required mechanical properties such as structural stiffness[12]. Hence, interest has grown in lightweight and energy absorbing lattices. The fabrication of lightweight SLM Ti6l4V alloy micro-lattice structures was studied by Campanelli et al. [13]. Compression tests were performed to evaluate the mechanical strength and the energy absorbed per unit mass of lattice truss specimens – Specific Energy Absorption (SEA). The Taguchi optimization method has shown the correlation between maximum load capability and maximum energy absorbed per unit of mass. Gorny et al. [14] used experiments to address the deformation and failure behavior of Ti6Al4V lattices produced by

SLM on the local scale. They demonstrated that the energy absorption of SLM heat-treated structures is higher than the energy absorption of untreated structures, due to a significant increase in ductility after heat treatments. Tancogne-Dejean et al. [15] reported an exceptionally high SEA for the SLM 316L alloy octet truss lattice. Their experimental study showed that the energy absorption of lattice materials shaped with cylindrical struts is among the highest of all shapes studied in their work. In addition, computational work showed that the energy absorption of lattice materials increases substantially with higher relative densities. Smith et al. [7] studied truss SLM 316L alloy unit cells. Two simple architectures, BCC and BCC-Z, were studied under compression. The energy absorbed by these unit cells was calculated based on the area under the force-displacement curve. In order to compare the energy absorbed by different unit cells, it was divided by mass - Normalized Energy Absorption (NEA). The initial stiffness, yield strength and energy absorbed were shown to be drastically improve by making the unit cell taller and narrower. Following these works, the impact response of AM 316L hybrid lattices fabricated by SLM were studied by Harris et al. [16]. Three structures tested using both static and dynamic experiments. Square honeycomb, lattice walled square honeycomb and a fine lattice square honeycomb. The square honey comb was found to be superior in terms of specific strength and SEA. An exceptional result occurred with the lattice-walled square honeycomb, which outperformed energy absorption efficiency (the ratio of energy absorption to maximum stress) at strain rate of $10,000/s$ compared to the square honeycomb. This result indicates a possible optimization in the dynamic intermediate regime. Lijun et al. [17] studied functionally designed graded Ti6Al4V, which are smart and continuous gradient lattice structures fabricated by SLM. Static and dynamic tests, along with FE analyses, showed that graded lattices exhibit excellent mechanical properties, including energy absorption. Both energy absorption and collapse strength are higher compared to other uniform lattices. In addition, different load directions don’t seem to affect energy absorption for functionality lattices.

From the above brief survey, it appears that most recent research was conducted on the compressive response and energy absorption of complex AM lattices, and less was conducted on AM base cylindrical patterns, mainly under quasi-static loading. Additionally, the structure's energy absorption trend is still missing. Therefore, this paper will address the compressive response of various simple types of cylindrical printed structures, with emphasis on energy absorption.

2. Methodology

2.1. Case Study Determination

The case study consisted of two tubular and one columnar pattern, designed via literature review and preliminary numerical simulations. These patterns can only be manufactured using AM technology, due to their complex shapes and small size. Quasi-static and impact (dynamic) load tests were carried out in order to investigate strain rate dependency, mechanical response, failure mode, energy absorption, and for comparison with the printed solid reference cylinder. The designed patterns and bulk specimens were all manufactured at the same time. The test specimens (3 patterns and solid cylinder) were similar in quasi-static and dynamic experiments. Two constraints were defined in order to compare patterns:

1. Constant common cross-section:

$$C_1 = A_{total} = \sum_{i=1}^{m} A_i \tag{1}$$

The common cross section indicates that the section is constant along cylindrical axis. Where, A_i is the element i cross section area. By summing areas with index i to m, the total area for the C_1 was

calculated. For the tubular patterns the total area defined the patterned cross section area, while for the columnar pattern the total area is the sum of the columns' cross-section areas.

2. Constant mass:

$$C_2 = m_i = m_{i+1} = \ldots = m_k \tag{2}$$

Where, m_i is the mass of specimen i, while k is the total number of the elements in the specimen.

2.2. Test Specimens

The specimens were fabricated using EOS M280 Direct Metal Laser Sintering (DMLS) machine. The laser power was 200W and the hatch spacing used the EOS default parameters (EOS proprietary information). The Ti6Al4V powder was deposited in 30μm layers prior to each laser scan and the build platform was held at 35ºC during specimen production. The specimens' limiting dimensions were 9mm in diameter and 9mm in length. These dimensions were chosen according to published recommendations for dynamic compression tests [18], and are summarized by three main ratios in relation to the apparatus bars and specimen dimension's. The ratio between the apparatus bar length and diameter (L/D), should be at least by an order of 20. The ratio between the apparatus bar diameter and specimen diameter (D/d_0), is within a 2-4 range, and the ratio for the specimen length to diameter (l_0/d_0) should be 0.5-1. The recommended ratios and specimens' compliance are shown in **Table 1**. The columnar pattern (8-Column) **Fig. 1(a)-(b)** represents and examines vertical columnar structures, constructed of uniformly distributed columns. The first tubular pattern (Tube I) **Fig. 2(a)** explores the tube's elastic-plastic collapse, constructed with the same outer diameter and tapered inner profile (tailored edges to enhance the collapse failure mode). The second tubular pattern (Tube II) **Fig. 2(b)** explores a geometrical stiffened structure, made of adjusted internal and external diameters. Additionally, extra material ("disks") was added at both ends of the patterns

gripping the columns and the tubular patterns. Those "disks" were designed to achieve maximum stiffness and to avoid unintended loading while conducting the compression tests. The specimens and cross sections are shown in **Figs. 2(a)-(c) and 3(a)-(b),** respectively. The pattern characteristics and dimensions are summarized in **Table 2.** Additionally, detailed specimen dimensions are shown in Appendix **A Fig. 1-4.**

	L/D **[mm\mm]**	D/d_0 **[mm\mm]**	l_0/d_0 **[mm\mm]**
Recommended dynamic ratios	**>20**	**2-4**	**0.6-1**
Dimensional compliance	**57 (1100/19.3)** **31 (605/19.3)**	**2.14 (19.3/9)**	**1 (9/9)**

Table 1 Dynamic recommended ratios and the specimen dimensional compliance for compression experiments

L and D indicate the length and diameter of the bars, respectively. l_0 and d_0 indicate the initial specimen length and diameter, respectively.

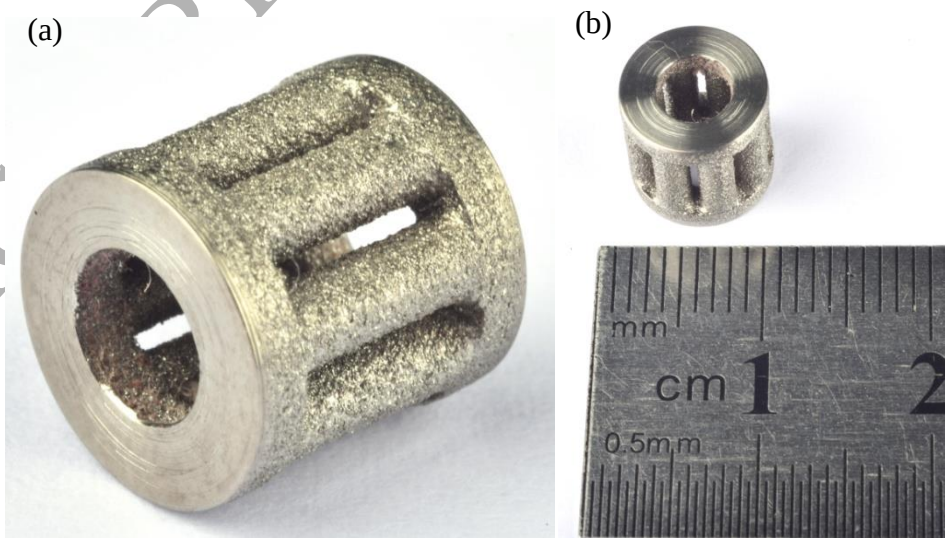

Figure 1 Specimen 8-Column (a) isometric view, (b) pattern 9x9mm scale

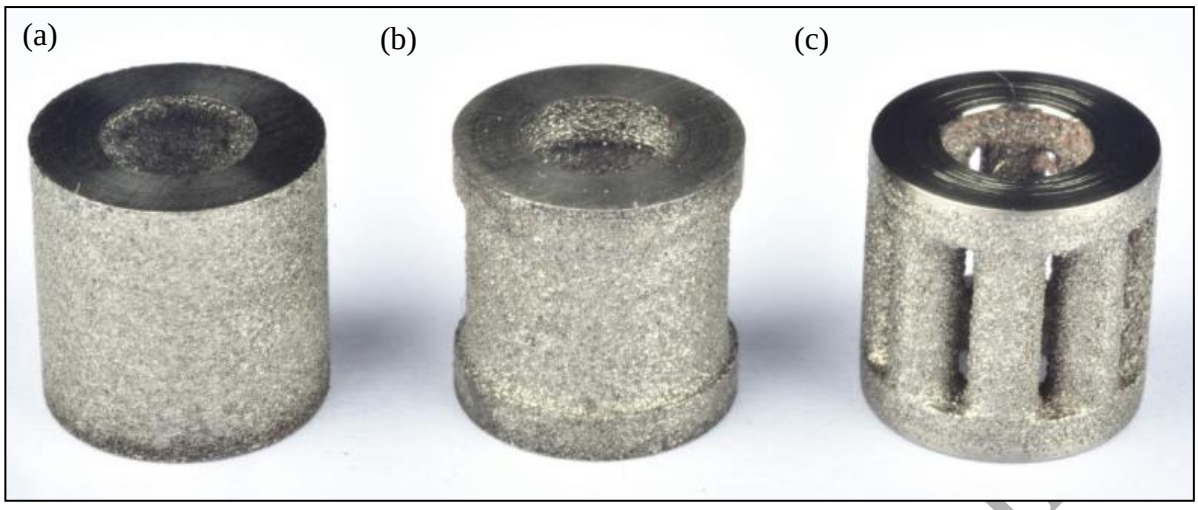

Figure 2 Patterns (a) "Tube I", (b) "Tube II" and (c) "8-Colum"

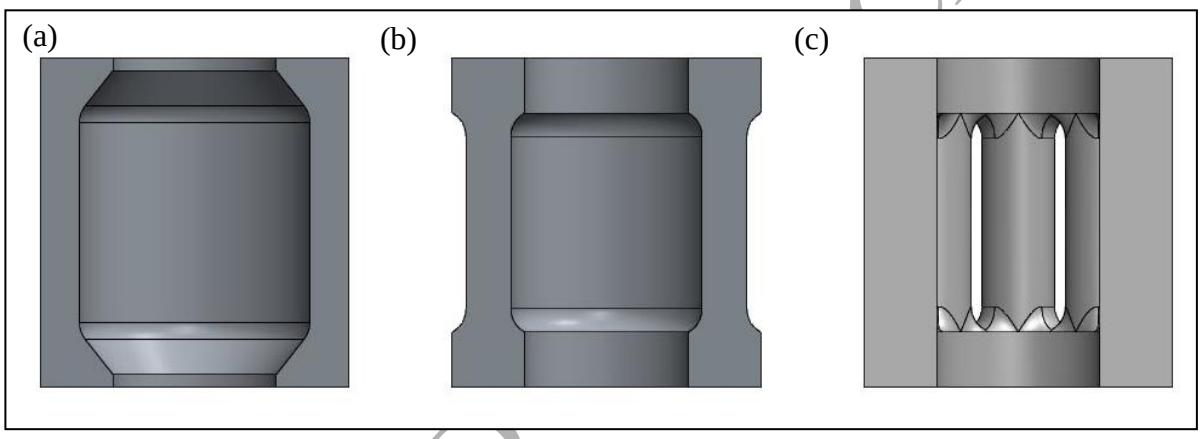

Figure 3 Patterns cross-section (a) "Tube I", (b) "Tube II" and (c) "8-Column"

Pattern	Diameter [mm]	Length [mm]	Inner Diameter [mm]	Outer Diameter [mm]	Mass [g]	Cross-Section [mm^2]
8-Column	9	9	4.8	9	0.8	28.2
Tube I	9	9	6.7	9	0.8	28.2
Tube II	9	9	5.6	8.2	0.8	28.2
Bulk	9	9	---	9	2.5	63.6

Table 2 Patterns characteristics and dimensions summary; green indicates patterns constraints, while red refers to the cylindrical bulk specimen

2.3. AM Pattern Production

During samples production, some difficulties arose related to process and geometry. In the SLM process, the products are assembled over a tray, and are bonded to it. Specimens' fabrication along the cylindrical axis prevented any discrepancy related to different building orientation. Later measurements of height (mainly affected by finish operation than building capabilities of SLM) and non machined outer diameter showed a small standard error from the required dimensions of 9±0.05mm. For height and diameter, the mean and standard error values were 9.01±0.005mm and 8.98±0.005mm, respectively. In order to reduce residual stress during the process, performing heat treatment is recommended. Vrancken et al. [19], recommended heat treatment for Ti6Al4V, and this was applied to the manufactured specimens. The parts were heated to $650°C$ for 2 hours in a vacuum furnace, followed by air cooling to room temperature. Afterwards, the products were removed from the tray, cut and polished on both sides. Those steps were required to minimize friction during compression tests. In addition, manufacturing the specimens must include extra material for erosion cutting (wire cutting) from the tray, and guarantees symmetrical and identical disks on both sides. The manufacturing difficulties were solved by adding two layers to the specimen. The first for fine engraving, by adding a 0.2mm thick layer of to both sides of the disks, shown by the red marking in **Fig. 4.** The secondly for coarse grinding, by adding a 1mm thick layer of material of smaller diameter to both sides, shown by yellow marking in **Fig. 4**. Regardless of the length cut from the tray, the coarse layer (yellow) ensured that the operator has extra material to remove. Afterwards, when the operator reached the fine layer (red), the machine was set to cut the 0.2mm thick layer accurately. Finally, both external surfaces were polished to minimize friction, which enabled the specimen's free radial expansion during compression tests. The described process proved to be both easy and accurate according to later measurements. It is important to note that other specimens' dimensions are "as built" (meaning no additional machining).

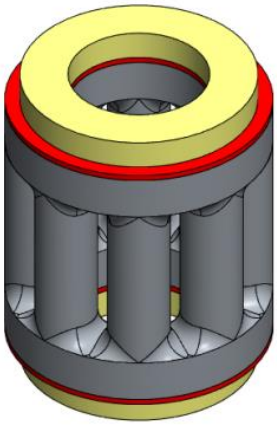

Figure 4 Example of specimen "8-Column" with extra material yellow layer (coarse) and red layer (fine)

3. Experimentation

AM Ti6Al4V patterns were tested under compression using quasi-static and dynamic regimes. The tests include bulk printed specimens for comparison. In terms of repetitions, experiments were carried on five samples at least, for each specimen condition. An example of one batch of patterns is shown in **Fig. 5(a)-(b).** For quasi-static test the strain rate was $\dot{\varepsilon} = 0.001$ /s, and the dynamic tests were within a range of $\dot{\varepsilon} = 2,000 - 3,500$ /s. For these tests, the dynamic deformation pattern was recorded using a digital high-speed video camera (Kirana).

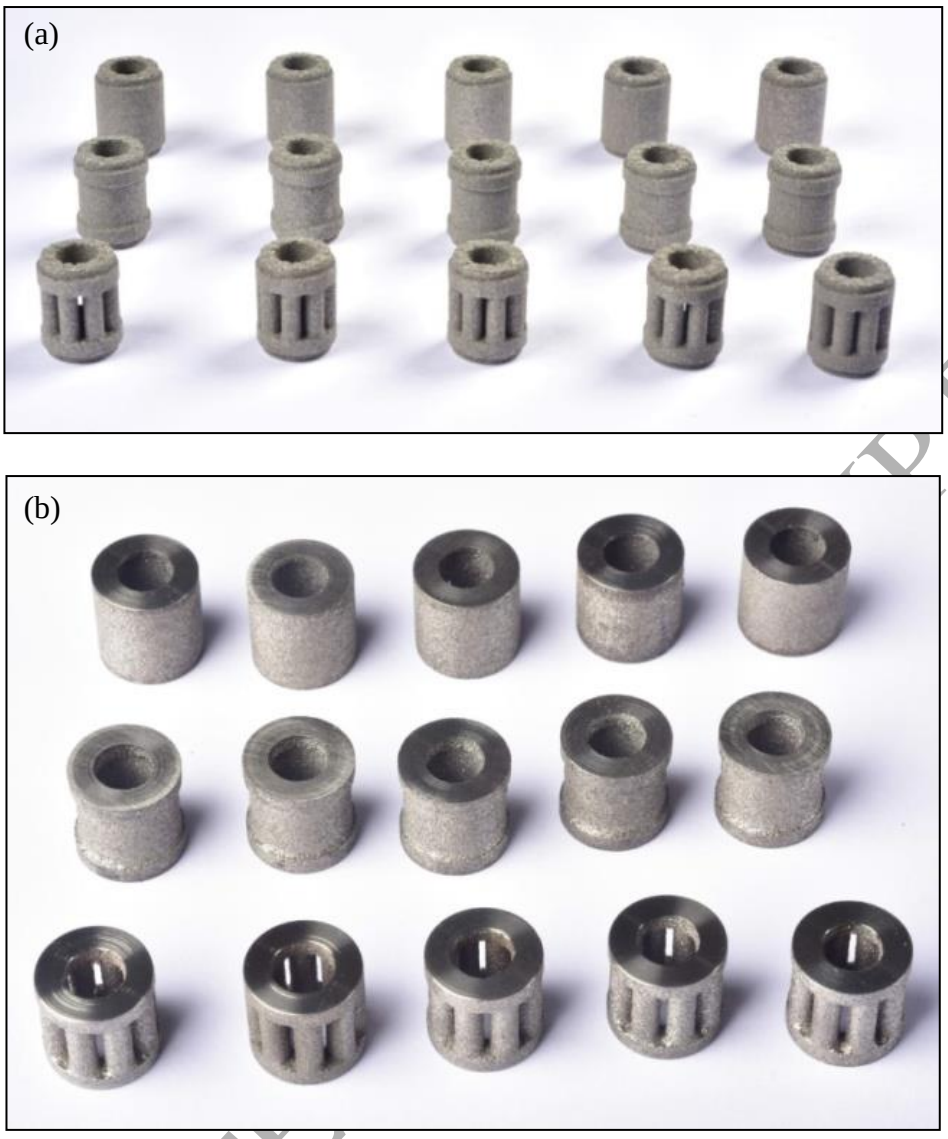

Figure 5 Three discrete patterns batches (a) batch taken from AM tray (b) batch after post processing

3.1. Quasi-Static Compressive Response

Experiments were carried out using a screw-driven INSTRON model 4483 machine at room temperature, operated under displacement control. The test strain rate was $\dot{\varepsilon} = 0.001/\text{s}$, complying with the ASTM E9 standard for circular shapes [20]. The displacement was measured using a laser extensometer with a gauge length of 5mm, and an ALLIED camera was used to record the compressive deformation response. The experimental data was integrated into MATLAB algorithm in order to calculate the force and NEA vs. displacement. The specimens' displacement Δ was

calculated by subtracting the displacement of the outer surface U_{out} from the displacement at the entrance U_{in}, and is produced by:

$$Displacement(\Delta) = U_{in} - U_{out} = U_{in} \qquad , U_{out} = 0 \tag{3}$$

U_{out} is equal to zero due to fixed plates in the compression quasi-static apparatus. The force F was obtained directly from measurements during experiments, while the energy absorption was calculated via trapezoidal integration of the force vs. displacement graph. This was done using two indexes, i for location and j for summary. Finally, the energy absorption was normalized by dividing it by the specimens' mass m_{sp}. This is defined as NEA, and is given below:

$$NEA = \frac{1}{m_{sp}} \sum_{J=1}^{N} \frac{(F_j + F_{j+1}) \cdot (\Delta_{j+1} - \Delta_j)}{2} \tag{4}$$

Energy normalization has enabled the comparison of designed specimens to bulk. Good repeatability was measured during experiments, resulting in small standard deviation and error from the mean. The graphs obtained for force and NEA are shown for mean values in **Fig. 7** and **Fig. 8** respectively. As can be seen in **Fig. 7**, the maximum peak force among the patterns was achieved by the Tube II pattern, which was accompanied by a drastic decrease after the peak. The minimum peak force is achieved by 8-Column. The tendency in Tube I was different compared to the others, as it was the combination of peak plateau force with extended displacement. By integrating the Tube I curve, the maximum absorption among patterns was obtained. This pattern absorbs, in total, more than 85% compared to 8-Column, more than twice of Tube II, and more than 15% compared to the bulk specimen. Remarkably, Tube I absorbs enhanced energy from the start to the total. It is notable that all patterns show enhanced energy absorption to a displacement of 1.2mm compared to the Bulk's specimen geometry. But beyond this, the graphs differ drastically as a result of different failure modes.

The differences in failure modes at given time intervals are shown in **Fig. 9**. The Tube I pattern experienced the largest deformation and delayed failure more than the other geometry. Tube II deformed the least in total and failed immediately. The failure mode for Tube I was an axisymmetric elastic-plastic collapse followed by failure, while with Tube II it was a slight expansion followed immediately by shear failure. Additionally, by comparing Tube I to the 8-Column, a similar failure mode can be seen. Both experience elastic-plastic collapse followed by failure, but while Tube I experiences axisymmetric collapse, 8-Column experiences asymmetric collapse. The collapse mechanism can also be seen by the decreasing graduate force in the force-displacement curve in **Fig. 7.** 8-Column experienced asymmetric collapse and low critical force, and was therefore expected to absorb low energy levels. On the contrary, it experienced a large deformation after peak force accompanied by decreasing graduate force and total failure delay. The result was an average NEA (total), higher than Tube II and lower than Tube I. Hence, failure delay due to asymmetric collapse (8-Column) was found to be favorable compared to shearing (Tube II), but less favorable than axisymmetric collapse (Tube I).

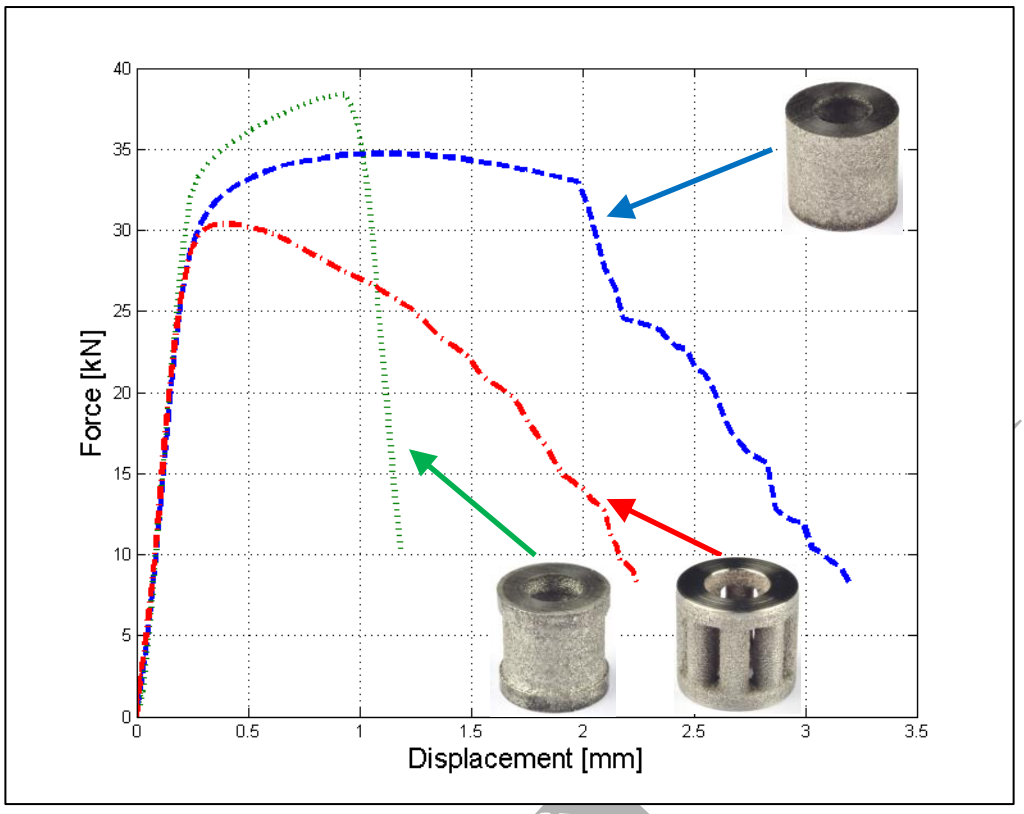

Figure 7 Force vs. displacement curves under quasi-static loads

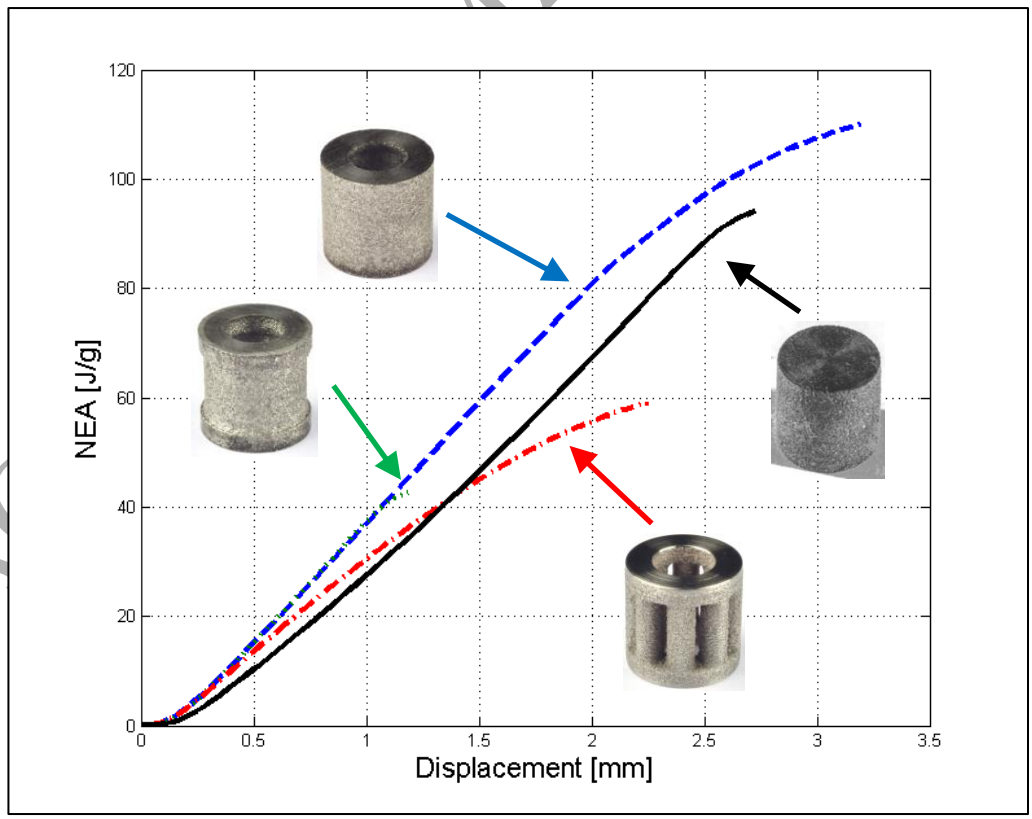

Figure 8 NEA vs. displacement curves under quasi-static loads

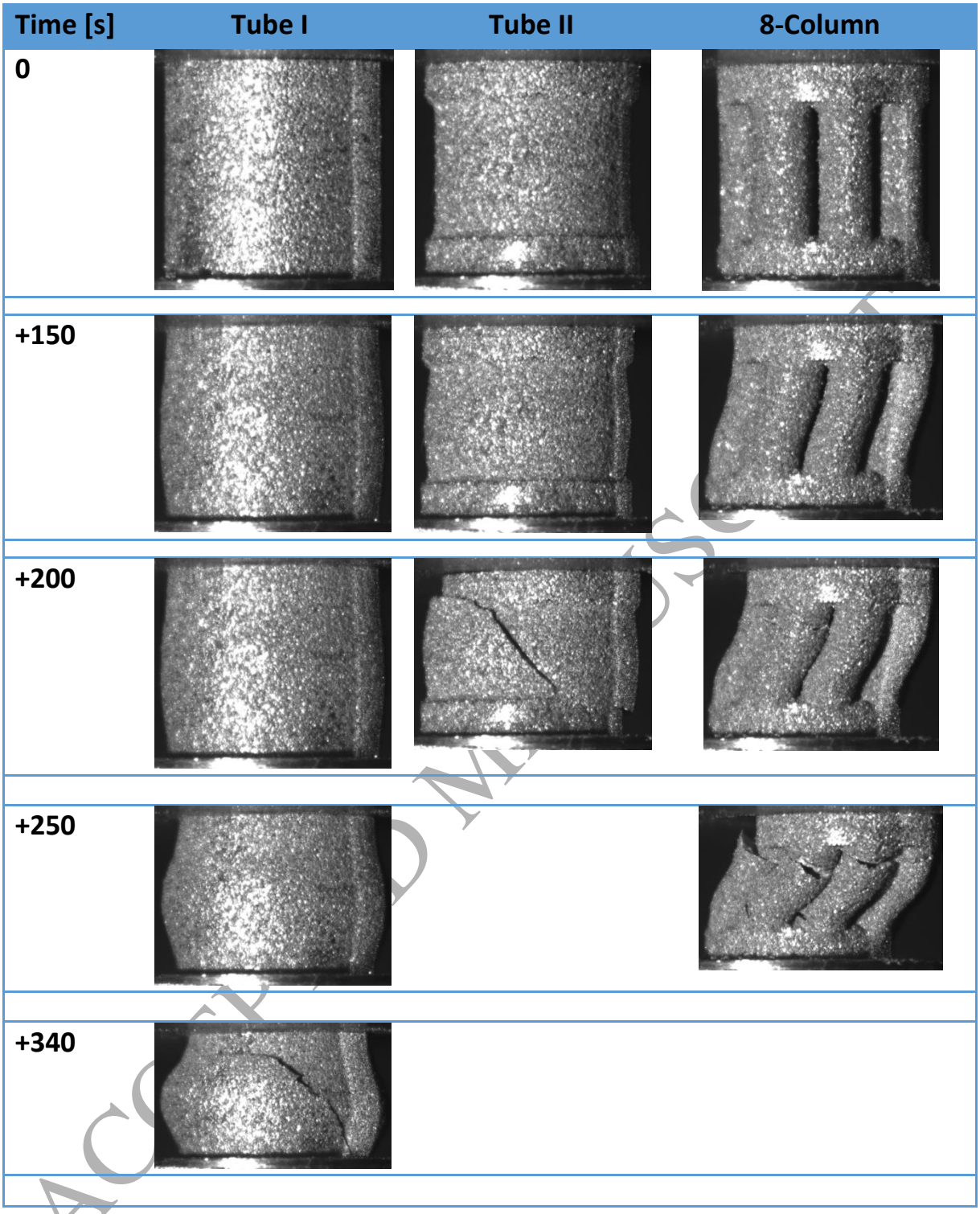

Figure 9 Variation of failure modes at given time intervals under quasi-static loads

AM Ti6Al4V can be classified as a ductile material, which undergoes significant plastic deformation by shear prior to fracture. This was reported to occur while conducting quasi-static compression experiments for bulk cylindrical Ti6Al4V specimens, by Fadida et al. [21]. This type of failure has

also occurred in Tube I and Tube II patterns, and is shown in **Fig. 10(a)-(c)**. For the 8-Column pattern, elastic-plastic collapse has caused stress to concentrate at the base columns where they connect to the disks, leading to crack development. Remarkably, the disks were shown to be as stiff as intended, thereby causing crack offsetting when reaching the pattern edge **Fig. 10(b).**

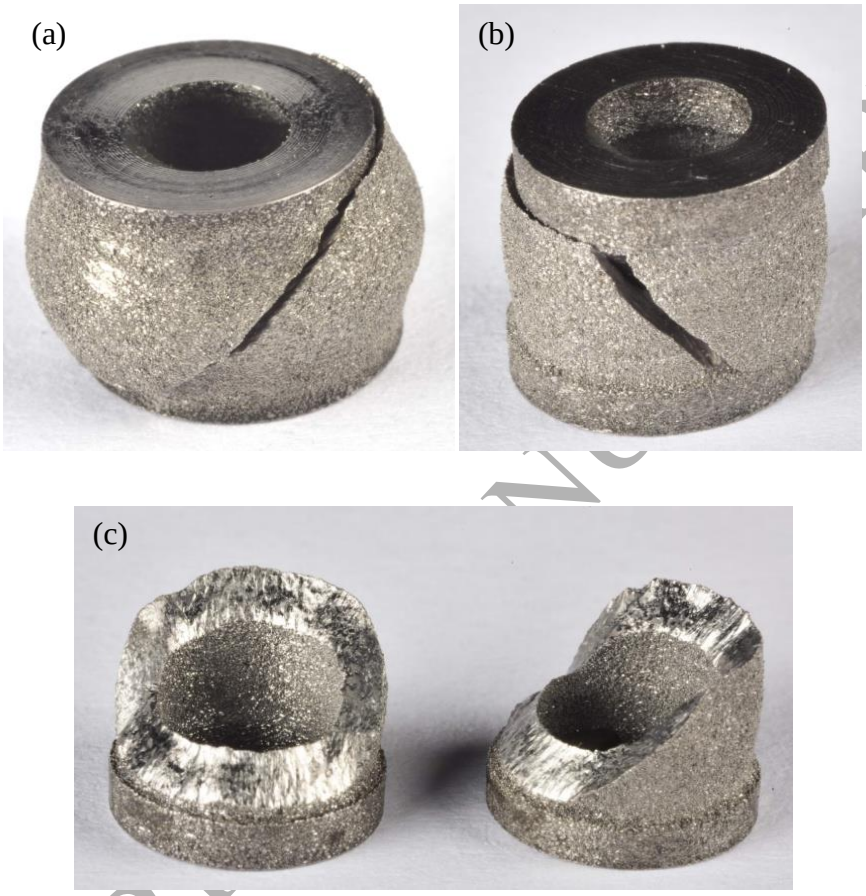

Figure 10 Quasi-static shearing failure, (a) Tube I, (b) Tube II and (c) Tube II, two separate parts

3.2. <u>Dynamic Experiment Results</u>

Experiments were carried out using a 19 mm diameter C300 maraging steel Split Hopkinson Pressure Bar (SHPB) apparatus, also known as a Kolsky Bar. This is a common test for high strain rates, within the $\dot{\varepsilon} = 100 - 8{,}000 / s$ range, for compression and tension [18,22]. To perform dynamic experiments, the striker impact velocity was controlled to induce strain rates within the $\dot{\varepsilon} = 2{,}000 - 3{,}500 / s$ range. During the experiments, two oscilloscope channels were used simultaneously to store measured strains at different locations. The incident strain was measured at

540mm from the specimen-bar interface, and the transmitted, at 240mm. In addition, the compressive response was recorded during experiments using a Kirana camera with a long range microscope lens. A total of 180 pictures were recorded in each experiment, with a frame resolution of 924x768pixel captured at a framing rate of 500,000fps. Lighting was provided by a pair of xenon flashes. The experimental data was integrated into a MATLAB algorithm to calculate the displacement, forces and NEA. The expressed displacement for dynamic experiments was similar to the quasi-static, which was given in **Equation 1**. With dynamic conditions, the outer surface displacement value was none zero, which differs from quasi-static, and is produced by:

$$Displacement(\Delta) = U_{in} - U_{out} \tag{5}$$

One-dimensional elastic wave propagation in bars theory was used for calculating forces at the specimen's entrance and outer surfaces F_{in} and F_{out}, respectively. These are produced by:

$$F_{in} = A_b E_b (\varepsilon_i + \varepsilon_r) \tag{6}$$

$$F_{out} = A_b E_b (\varepsilon_t) \tag{7}$$

Here, bar strains are for the incident ε_i, for the reflected ε_r, and for the transmitted ε_t, where A_b and E_b were the bar cross section area and young's modulus, respectively.

A state of equilibrium is achieved after several reverberations, once the specimen is deforming in a uniform manner, implementing the following:

$$F_{in} = F_{out} = F \tag{8}$$

The NEA was calculated from displacement Δ and force F, according to **Equation 2.** Good repeatability was measured during experiments, resulting in small standard deviation and error from the mean value. The graphs obtained are shown for mean values of force and NEA in **Fig 11(a)-(b)** and **Fig 12(a)-(b),** respectively. Tube II and 8-Column achieved the maximum peak force and a drastic force decrease, while Tube I achieved the maximum displacement with peak plateau force, as

shown in **Fig. 11(a).** When strain rate was increased from 2,000/s to 3,500/s, the resembled tendency was maintained, as shown in **Fig. 11(b).** The dynamic force curve for the 8-Column differs significantly from the one obtained in the quasi-static state. During dynamic testing, a drastic decrease in the force occurred. While in quasi static conditions, a gradual decrease in the force occurred. Hence, the dynamic compressive response was different from that obtained under quasi-static conditions. In addition, the columnar pattern was shown to be an outstanding structure compared to Tube II for the dynamic regime. It has the same force vs. displacement tendency, but sustains greater deformation, resulting in better energy absorption capability.

The NEA of up to 1mm pattern displacement was found to be higher than the Bulk specimen. Similar to quasi-static results, Tube I dominance is kept all the way until total failure. As seen in **Fig. 12(a),** Tube I can absorb 30% more energy in total than the Bulk specimen, almost twice as much as Tube II, and more than 120% compared to the 8-Column. When increasing strain rates from 2,000/s to 3,500/s (up to 0.8mm deformation), the 8-Column pattern absorbs more energy compared to the others, as shown in **Fig 12(b).** From this value and to failure, Tube I maintains dominance. Unexpectedly, the total NEA decreased from quasi-static to dynamic tests for all patterns (including the Bulk specimen). This fact apparently is related to the inertial effects, which cause relatively smaller displacement under dynamic conditions to total failure.

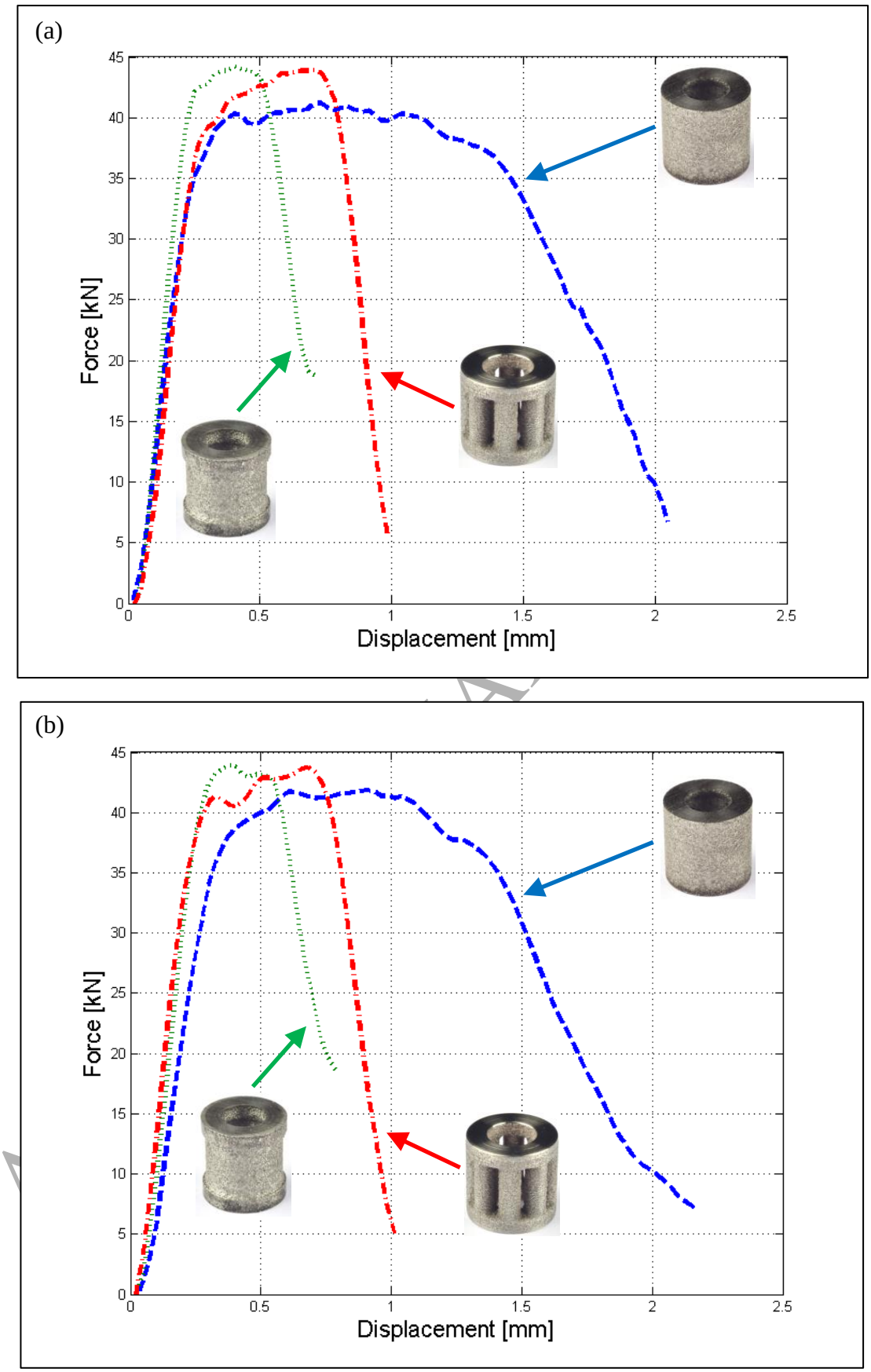

Figure 11 Dynamic force vs. displacement curves (a) nominal strain rate of 2,000/s, (b) nominal strain rate of 3,500/s.

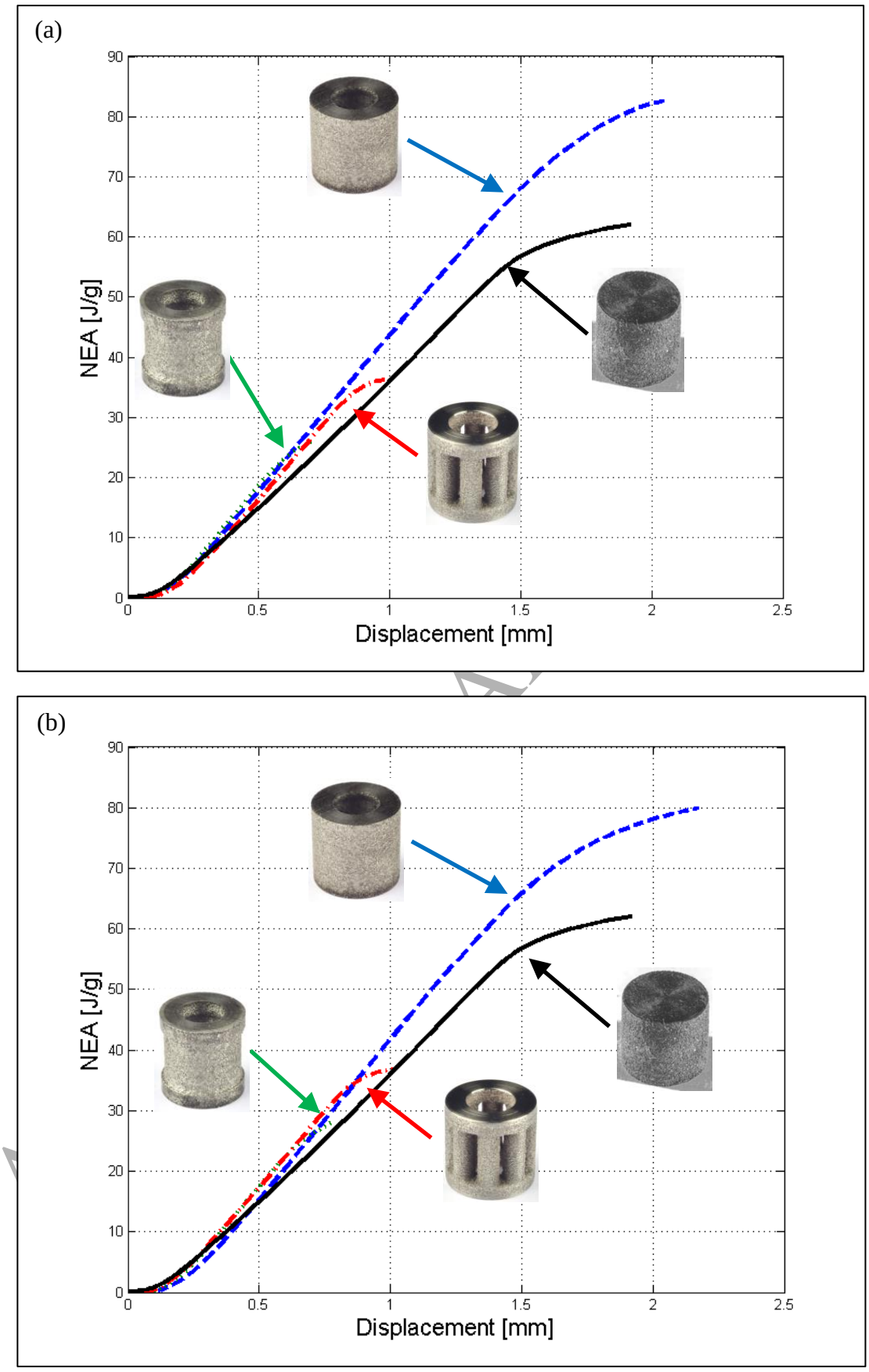

Figure 12 Dynamic NEA vs. displacement curves (a) nominal strain rate of 2,000/s, (b) nominal strain rate of 3,500/s.

Differences in failure modes at a nominal strain rate of $2,000/s$ at given time intervals are shown in **Fig. 13.** Tube I experienced the largest total deformation, which consisted of an axisymmetric elastic-plastic collapse, followed by failure. This was dissimilar to Tube II and the 8-Column pattern, which first expanded, and then immediately failed through the shearing mechanism. The failure modes for the patterns under dynamic conditions were similar to quasi-static conditions, with the exception of the columnar pattern. During quasi-static tests, the 8-Column pattern experienced asymmetric elastic-plastic collapse, while during dynamic testing, it experienced a slight expansion, and then immediately cracked near the connection to the disks. At first glance, the crack was suspected to be a result of stress concentration, which was located at the columns' connections to the disks. By zooming in to the crack area, it was evident that the shearing occurred near the end of the column, which can be seen in **Fig. 14.** The change in failure mode is suggested to be related to geometry, namely inertia effect. Inertia effect plays a significant role in dynamic enhancement of cellular materials, such as tetrahedral truss core lattice structures [23]. In addition, due to strain hardening, the columns buckle under impact later than under quasi-static conditions (meaning that. the critical buckling force increases at the columns). As seen in **Fig 15**, comparison between dynamic and quasi-static forces indicates a significant force increase for the columnar pattern in dynamic tests. Note that as the inertia effect and strain hardening is a possible suggested reason for the increase in force, a continuum-based quantitative examination of this phenomenon should be performed.

Shear failure occurred for all patterns under dynamic conditions compared to quasi-static conditions. The change within the failure mode of the 8-Columns pattern has contributed to shearing failures in dynamics.

Time[μs]	Tube I	Tube II	8-Column
0	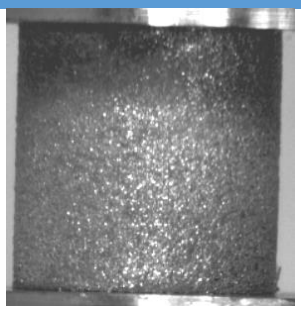	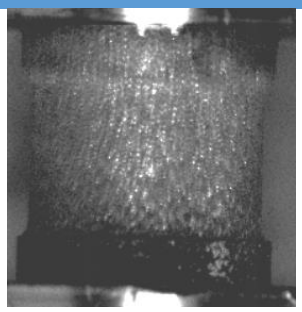	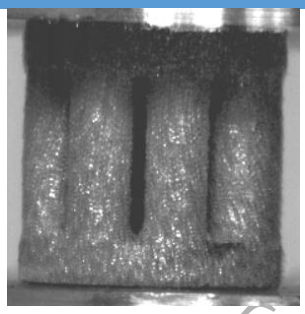
+25	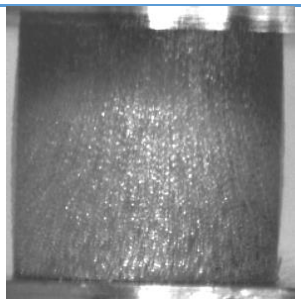	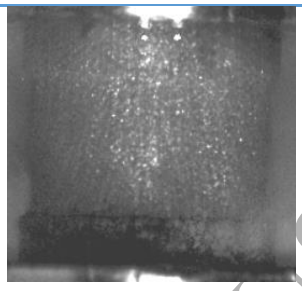	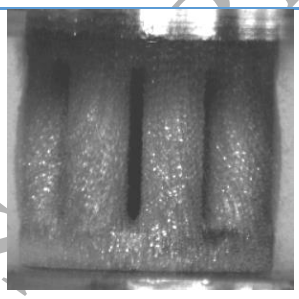
+75	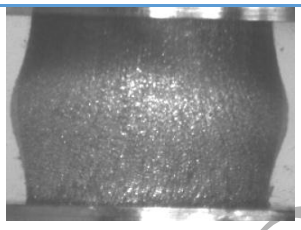	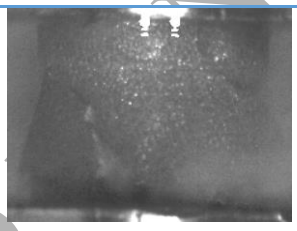	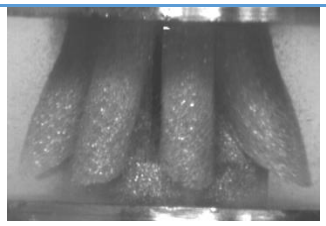
+100	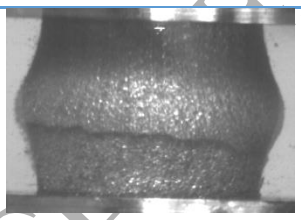	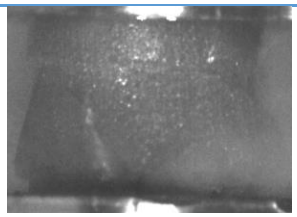	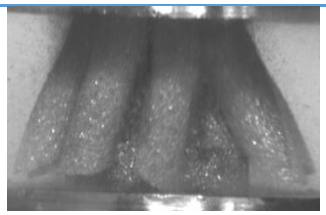
+125	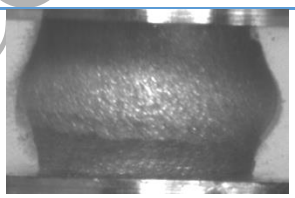		

Figure 13 Variation of failure modes at given time intervals under a dynamic strain rate of 2,000/s.

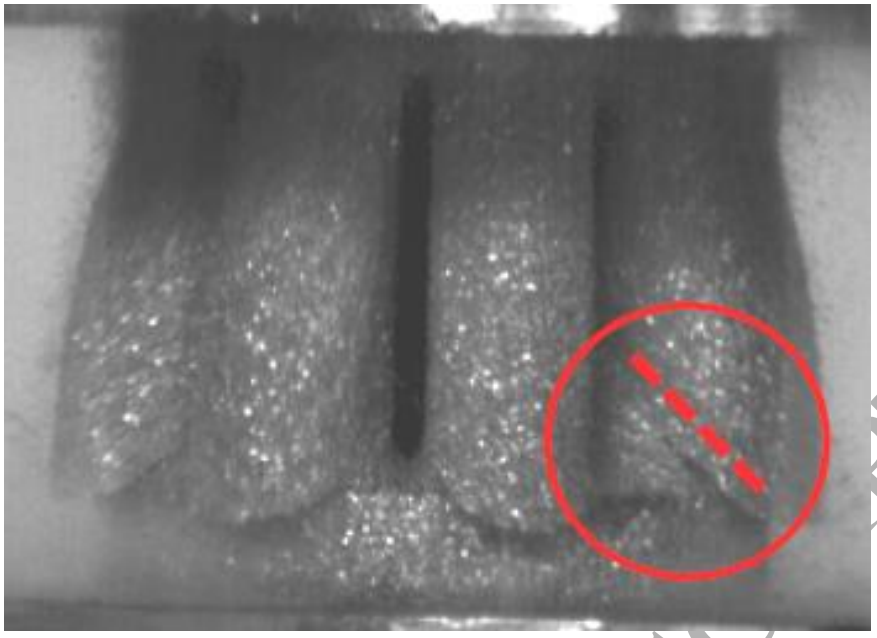

Figure 14 8-Column shearing

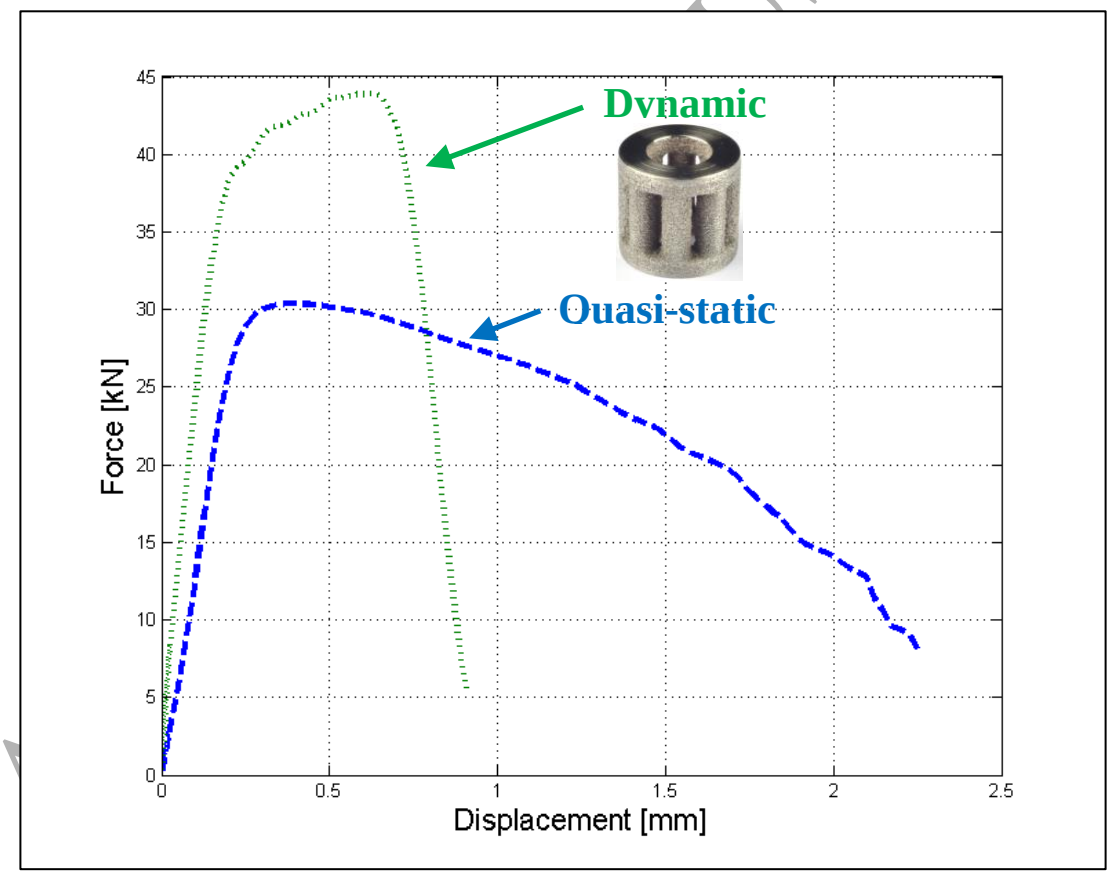

Figure 15 8-Column dynamic comparison of force vs. displacement to quasi-static

4. Numerical Simulations

Finite element analysis (FEA) was conducted with ANSYS workbench software, using an Autodyne explicit dynamics solver [24]. The basic mechanical properties were those of the Bulk specimen material, subsequently used for Tube I, Tube II and 8 Column.

The model considers large deformations and nonlinear material properties. A Ti6Al4V elastic–plastic model with failure was defined for this nonlinear simulation. Therefore, a three body model was built, which consisted of the incident and transmitted bars, with the compressed specimen in between the two. In addition, Coulomb frictional boundary contacts COF of 0.05 were implemented between the specimens' surfaces to the bars. Initial striker velocity was applied to the incident bar. This velocity was adjusted to match nominal strain rate of 2,800/s, according to the Bulk specimen experiment's.

The Hopkinson bars, Bulk, Tube I and Tube II were modeled with hexahedral elements (HEX8) and wedge elements (WED6). The columnar pattern is a 3-D shape which cannot be modeled by hexahedral elements due to geometry complexity. Hence, tetrahedral elements (TET4) were used to model this specimen. A uniform sizing mesh method was applied, which is critical for both time step control and accurate failure initiation. The max bars element size was 2mm while for the specimens it was 0.5mm. The generated mesh was checked for element quality (min 0.35 with average of 0.85), and for convergence (4 times smaller element with neglected results change).

The true stress-strain curve of AM Ti6Al4V was evaluated from dynamic experiments of cylindrical $\phi 9x9mm$ bulk printed specimens. Comparing with [21], the stress-strain curve obtained for cylindrical specimens ($\phi 7x7mm$), was very similar to the one obtained for our current dynamic experiments with $\phi 9x9mm$ specimens.

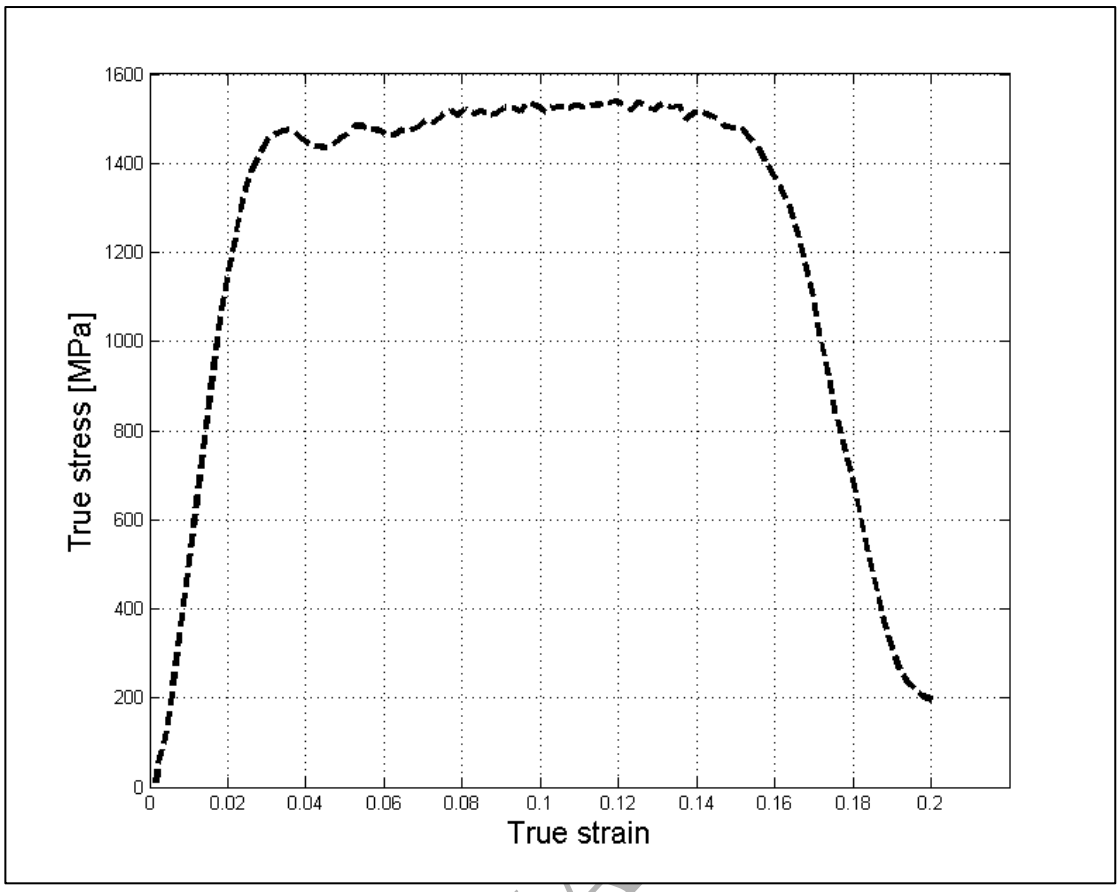

Figure 16 Dynamic true stress-strain for Bulk specimen, measured at nominal strain rate of 2,800/s.

The data for the elastic material properties were density ρ_s equal to 4428Kg/m3, Young's modulus E_s equal to 111.6GPa, Poisson ratio ν_s equal to 0.31 and yield stress σ_{y_s} equal to 1080MPa (0.2% of plastic strain). The plasticity material behavior used was isotropic with multilinear hardening. The material data was input in tabular form of plastic strain vs. stress. The points were extracted from the true stress vs. strain (**Fig 16**), and the first point was the yield stress with zero plastic strain. Regarding failure, the shear response was evident and dominant, hence a maximum shear strain failure criterion, with a value of 0.15 tensorial shear strain.

4.1. <u>Bulk Specimen Simulation Results</u>

The Bulk specimen was used for validating constitutive relation, and for calibrating boundary interactions of friction coefficient. First, a good match was achieved for this specimen both for force and NEA curves. Then, similar parameters were implemented to patterns Tube I, Tube II and 8-

Column, including maximum shear strain failure. **Fig. 17(a)-(b)** presents the numeric fit of Bulk specimen at a nominal strain rate of $2,800/s$, which was compared to experimental force and NEA results, respectively. The numerical force matched well with the experimental results both for plasticity behavior and for failure response, a slight difference was seen as the force reduces to zero value. The shear failure initiation and mechanism was well predicated by simulation (**Fig 18)**, which have also been reported in experiments on AM Ti6Al4V cylindrical specimens ($\phi 7x7mm$) under dynamic loading [21].

4.2. Tube I Specimen Simulation Results

The Tube I numerical model was adjusted to the experimental nominal strain rate of $2,000/s$, which was recorded at experiments. Hence, a lower striker velocity was applied due to its smaller cross section, compared to the bulk specimen. As seen in **Fig. 17(c),** the numerical model for the force-displacement curve had a good match for the plastic flow behavior, but not for failure, it has initiated much earlier than required (displacement of 0.8 vs. ~1.4 mm). When the force slightly reduces, shear initiates and cracks the simulated specimen, as opposed to experiments, there the force continues (plateau force). In addition, similar tendency occurred for the numeric NEA curve. It had a good match to experimental results until failure initiated. From there on, the numeric trend was found to differ from the experimental curve, as seen in **Fig. 17(d)**.

Later, the Tube I pattern numerical failure mode was compared to its experimental failure mode at given time intervals. As a result of early failure initiation, partial match was observed. However, the subsequent deformation pattern corresponding to elastic-plastic collapse was not well reproduced, as shown in **Fig. 19 (a).**

4.3. Tube II and 8-Column Specimens Simulation Results

Numerical simulations for Tube II and the 8-Column were conducted using similar analysis parameters as previous Bulk simulations. For those, good correspondence is shown by examining the

force and NEA graphs, as seen in **Figs 17(e)-(f) and 17(g)-(h).** The numeric failure modes for Tube II and 8-Column patterns were compared to experiments at given time intervals. This analysis confirmed a correspondence of deformation until fracture initiation, shown in **Fig. 19(b)-(c).** Remarkably, during the simulation, the fracture occurred at the right time, but the location and progress were different from those observed in the experiments. Tube II pattern simulation exhibited slight expansion and then immediate shearing located at the middle of the pattern (not near the disks). However, during experiments the fracture initiated near the disks. For the 8-Column pattern, during simulation, the shear failure occurred at the middle of the columns. By contrast, the experimental shear failure occurred near the disks and progressed by "folding fan" progress, which wasn't reproduced by the simulation.

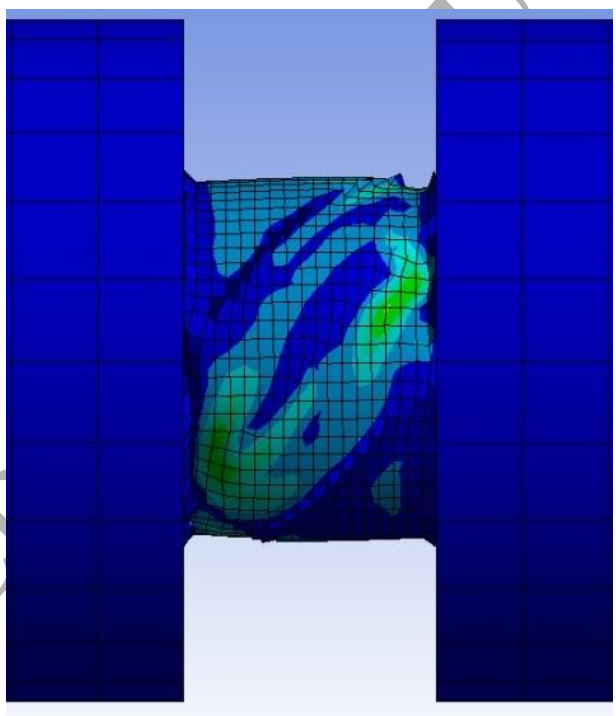

Figure 18 Bulk specimen simulation shearing failure

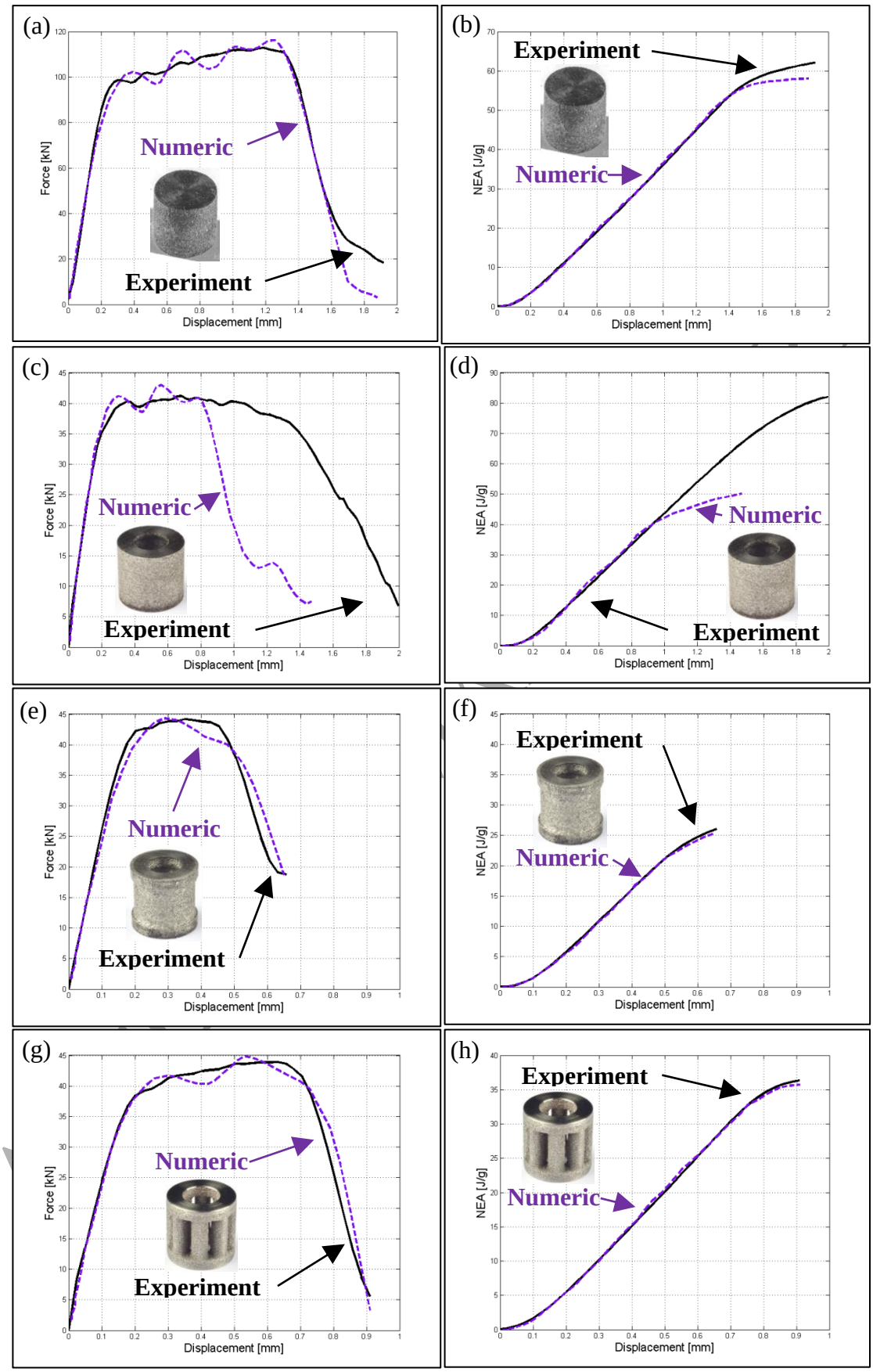

Figure 17 Dynamic comparison of experimental to numerical force and NEA vs. displacement (a)-(b) Bulk, (c)-(d) Tube I, (e)-(f) Tube II and (g)-(h) 8-Column

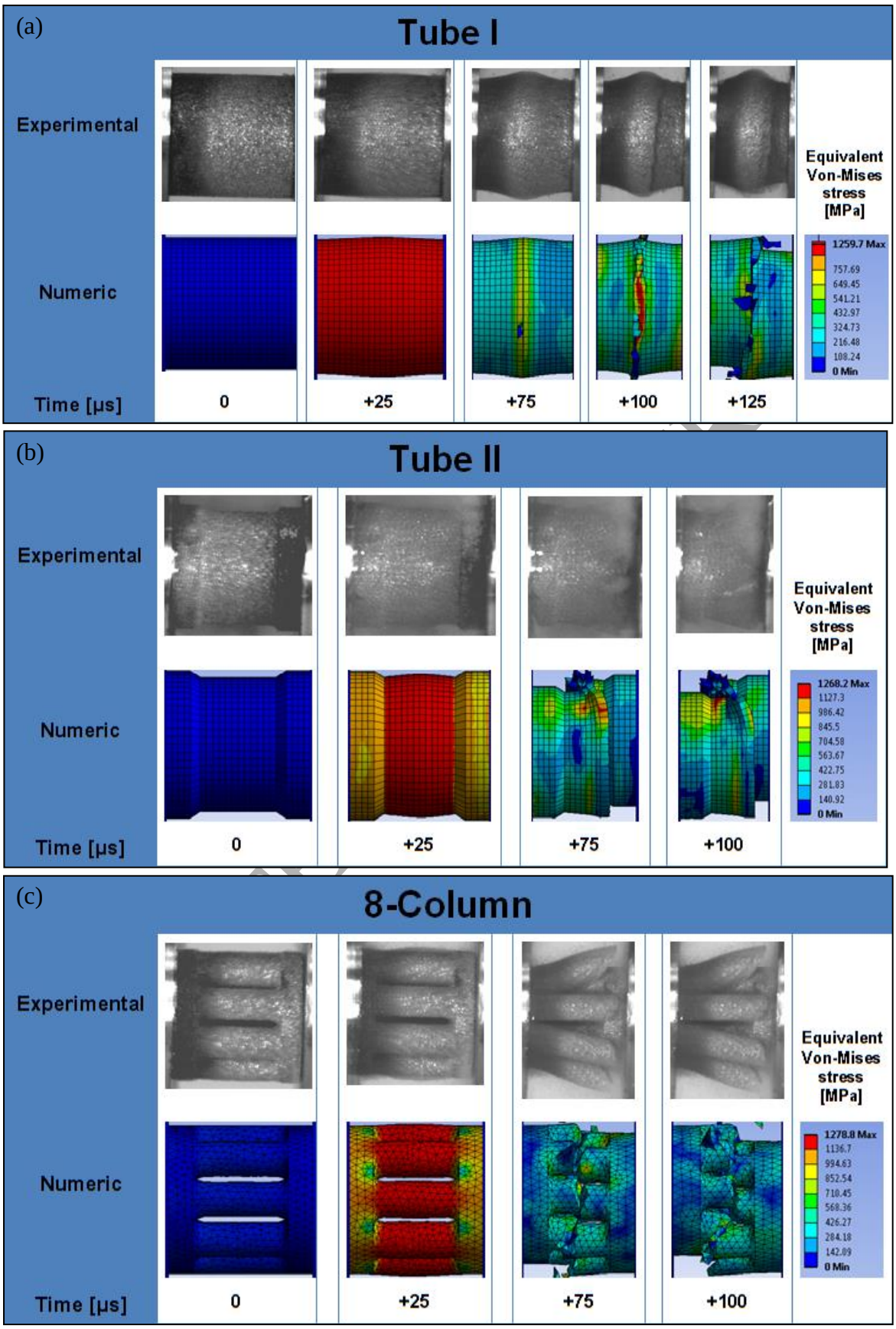

Figure 19 Dynamic comparison of experimental to numerical compressive response for patterns (a) Tube I, (b) Tube II and (c) 8 Column

5. Discussion

The quasi-static and dynamic experiments reported here provide new specific data for AM Ti6Al4V cylindrical patterns. The overall compressive behavior is shown to be strongly dependent on geometry and can be altered based on design. AM dynamic rate dependency of load-deformation characteristics had been previously identified and reported for AM Ti6Al4V by Ozdemir et al. [25] for lattice structures and Fadida et al. [21] for cylindrical dense and porous specimens. In this paper, tests were conducted within the $2,000-3,500/s$ range. The results support previous data and have expanded on load-deformation tendency of cylindrical patterns. At strain rates greater than $2,000/s$, the change in the flow stress-strain is negligible. Hence, the strain rate of $2,000/s$ will represent the high strain rate dynamics regime for cylindrical patterns. The transition from quasi-static to dynamic for displacement, force and energy absorption was primarily influenced by the inertia effect for the tubular patterns. However, for the columnar pattern, in addition to the inertia effect, the structure geometry was related to changes within the tendency, which can be seen for each pattern in **Fig 20(a)-(f)**. The transition from quasi-static to dynamic, results in higher peak force, lower displacement, lower energy absorption, and is summarized in **Table 4.** Regarding [13], a dissimilar conclusion was established. However, the structure that presented the highest load capability for lattice SLM structures had the highest energy absorbed per unit mass. For cylindrical patterns, the structure that presented the maximum load capability (Tube II and 8-Columns) was not the one that absorbed the highest energy. In particular, Tube I exhibited a peak plateau force which was lower in comparison with other patterns. Additionally, the peak plateau force was found to be a benefit in manner of energy absorption capability [26].

The columnar response and failure mode have changed from quasi-static to dynamic, as shown in **Fig 21**(a)-(d). The "folding fan" failure mode is believed to be the newly reported result of experimental study. The reason for this phenomenon could be related to the force increase (45%

more) at the transition from static to dynamic, significantly higher than other tested patterns. This indicates a combination of geometry, inertial effect and strain hardening, but a continuum-based quantitative examination for this phenomenon should be carried out to provide additional data.

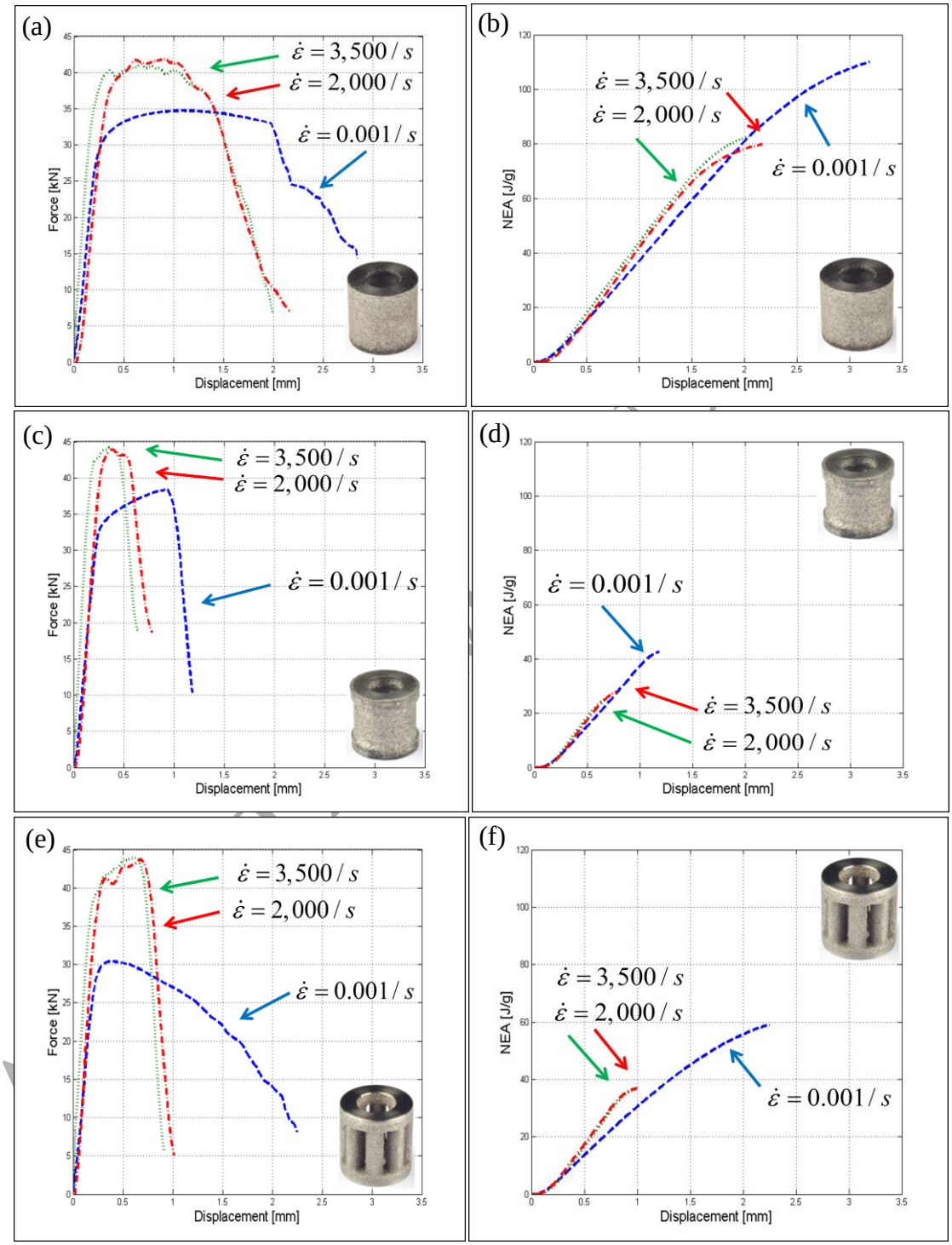

Figure 20 patterns force and NEA transition from quasi-static to dynamic (a)-(b) Tube I (c)-(d) Tube II and (e)-(f) 8-Column

	Quasi-static			Dynamic		
	Max peak force [kN]	Max displacement [mm]	Total NEA [J/g]	Max peak force [kN]	Max displacement [mm]	Total NEA [J/g]
Tube I	**35**	**3.2**	**110**	**42**	**2.2**	**82**
Tube II	**38**	**1.2**	**42**	**44**	**0.8**	**28**
8-Column	**30**	**2.2**	**59**	**44**	**1**	**37**

Table 1 Comparing quasi-static force, displacement and energy absorption to dynamic

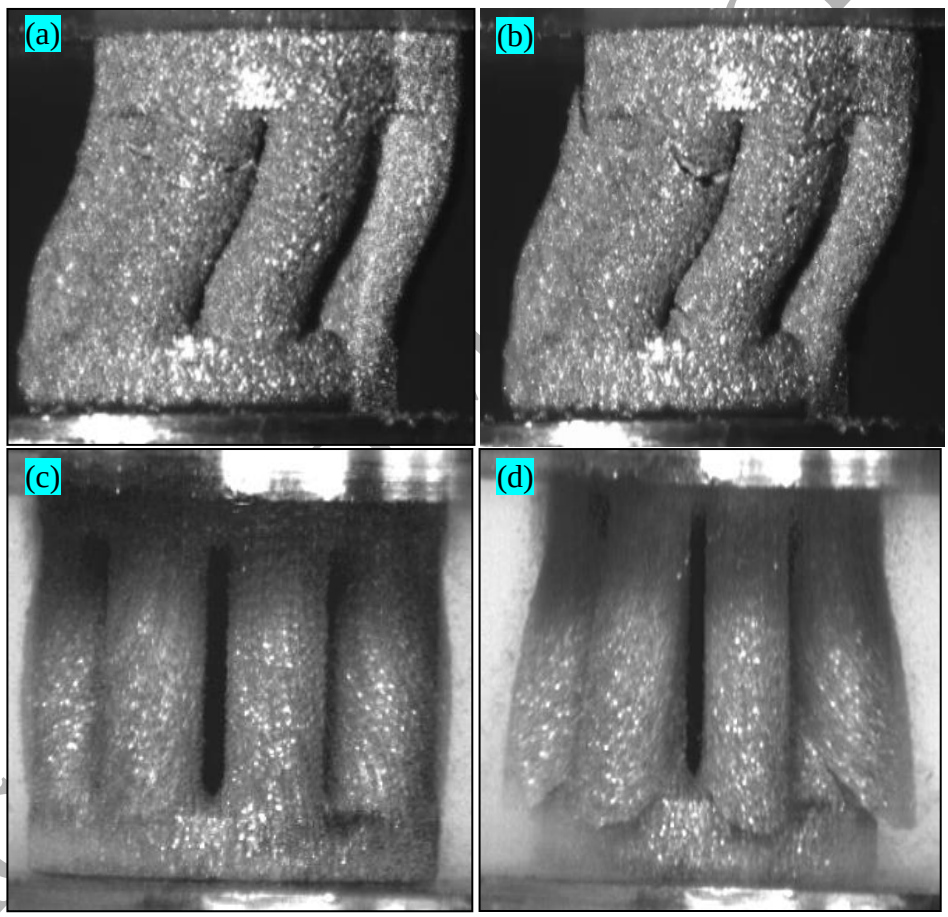

Figure 1 Columnar response (a) quasi-static before failure (b) quasi-static after failure (c) dynamic before failure (d) dynamic after failure

The energy absorbed by the pattern studied differs by accumulation and total value, which relates to its geometry and resulting failure mode. In order to examine these, the measured NEA was divided

into two steps: the 1st step, which determines the level up to the peak force (before failure is initiated), and the 2nd step, which determines the level from peak force to total failure (after failure initiation assumption). As shown in **Fig. 22(a)-(b),** within the 1st step, the bulk specimen absorbs significantly higher energy levels up to the peak, compared to the designed patterns.

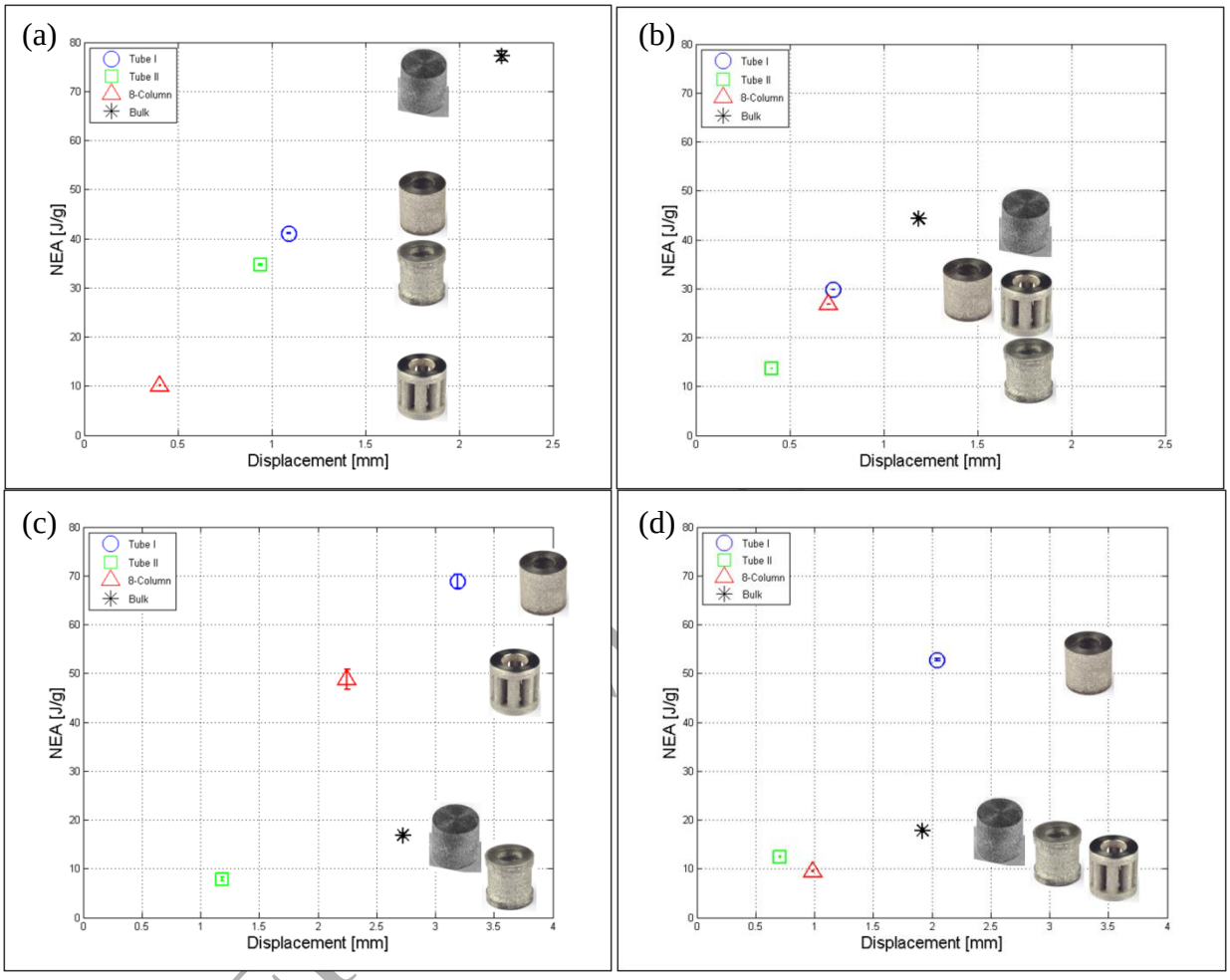

Figure 2 NEA steps (a) quasi-static 1st (b) dynamic 1st (c) quasi-static 2nd (d) dynamic 2nd

This advantage is due to the force-displacement monotonic raising tendency, shown in **Fig.23.** Here, the maximum is reached when close to total failure, meaning the failure is initiated at larger displacement levels compared to patterns, and transformation to dynamic has decreased the difference significantly. The dominant pattern for the 2nd step was the Tube I pattern, as seen at **Fig. 22(b) and (d).** This pattern absorbed enhanced NEA compared to the other patterns and to Bulk. This finding with the patterns' response seen in **Fig. 9** and **Fig.13,** shows the energy trend and failure

connection. It is impossible to completely prevent failure, however, delaying it has been shown to improve energy absorption, especially in the 2nd step (i.e. peak to total failure).

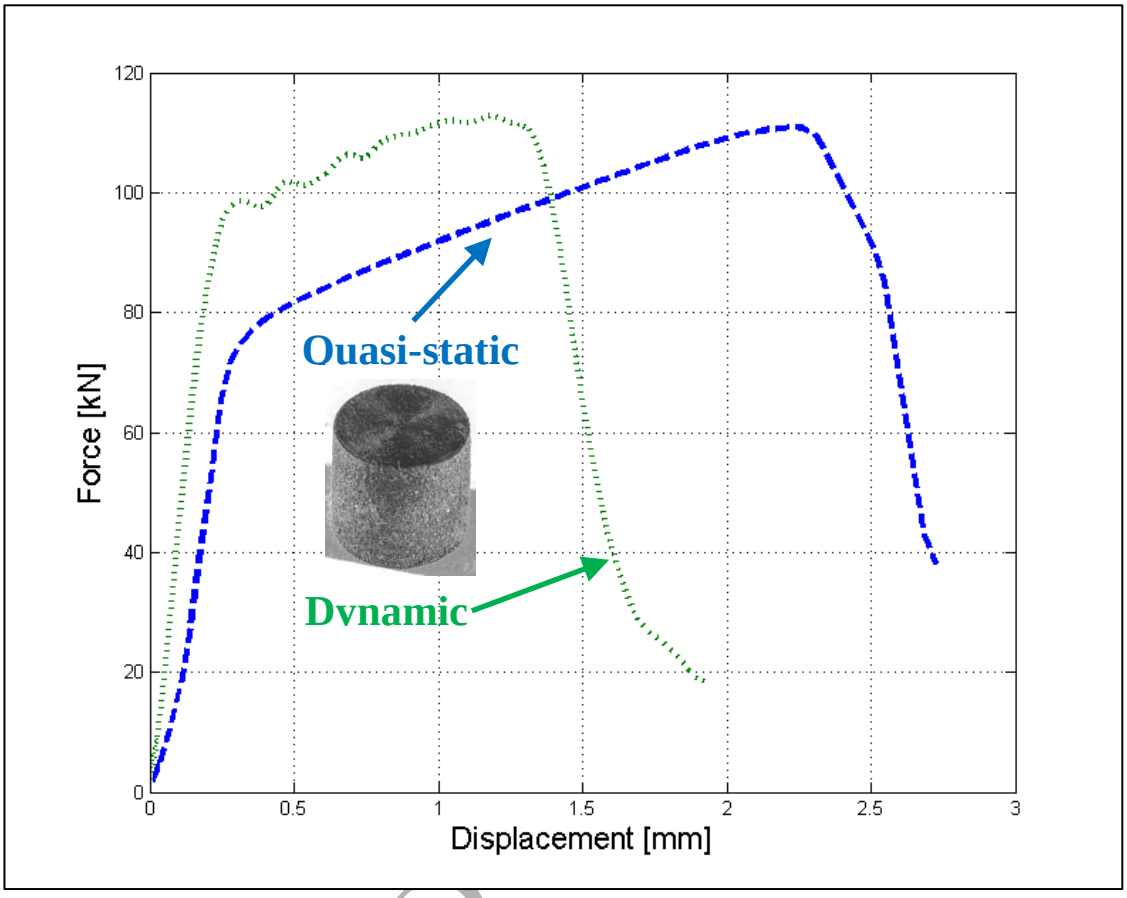

Figure 3 Quasi static and dynamic Bulk specimen force vs. displacement curves

The axisymmetric elastic-plastic collapse postpones failure efficiently, especially for the Tube I pattern. Similar results were introduced by Karagizova et al. [27], they reported that for cylindrical shells (none AM specimens) subjected to axial impact, larger amount of energy can be absorbed while exhibiting axisymmetric elastic-plastic collapse. In our study, the improvements for collapse mechanism were inserted into the Tube I inner profile, as seen in **Fig. 3(a)**. According to the results, the modified cross-section was a significant improvement. In addition, even an asymmetric collapse mechanism as seen at quasi-static conditions for an 8-Column pattern can improve energy absorption. The Tube II and 8-Column (dynamic regime only) were accompanied by high peak force,

and have encountered small displacement and resulting shearing failure. The columnar pattern was shown to be an upgrade and preferable geometry compared to Tube II when comparing the overall compressive performance.

The numerical results have shown an excellent fit for Bulk specimen compressive response, including failure initiation and progress using maximum shear strain criterion. In order to correlate patterns, a similar material behavior and failure were adopted. Those yielded good match for the plastic behavior, but overall poor match for failure initiation (Tube I), and poor match for failure location (Tube II and 8 Column). The discrepancy is most likely related to the selected failure criterion. It seems that additional work should be invested in optimizing the numerical simulation procedure and failure criteria, perhaps by considering the simultaneous operation of more than one such criterion, but this is beyond the scope of the present work.

Cylindrical discrete patterns have advantages over Bulk specimens, which makes it possible to select out features of the force-displacement and NEA easily based on the specific application needs. This is made possible due to the advantages of AM technology over other manufacturing methods, which can further enhance compressive behavior and energy absorption by topology means for Tube I inner profile. Strategically seeding local discrete patterns will obtain efficient and effective designs.

6. Conclusions

The compressive response, failure mode and energy absorption of AM Ti6Al4V cylindrical patterns were studied under quasi-static and dynamic compression experiments, in addition to numeric dynamic simulations. Particular emphasis is placed on the following findings:

- Comparing different Ti6Al4V cylindrical patterns constrained to similar mass and a common cross-section has been found to have strongly geometric connections, which influence the overall compressive performance including energy absorption.

- AM was shown once again to be unique technology for manufacturing tubular and columnar topologies, which can enhance mechanical compressive behavior.
- Compressive response of columnar pattern differs while comparing quasi-static to dynamic experiments.
- Failure mode of axisymmetric elastic-plastic collapse (Tube I) was found to be preferable trend for energy absorption.
- A isotropic multilinear hardening was found to describe satisfactorily the Ti6Al4V plastic behavior.
- A maximum shear strain failure criterion is not suitable to reproduce the failure mode of elastic-plastic collapse, although it matches well the Bulk specimen. Therefore, additional effort must be invested to solve this issue.
- Energy absorption can be controlled using AM discrete geometry design, which implies a potential for structural optimization.

7. Acknowledgments

This research did not receive any specific grant from funding agencies in the public, commercial, or not-for-profit sectors.

8. References

[1] S. Leuders, M. Thöne, A. Riemer, T. Niendorf, T. Tröster, H.A. Richard, H.J. Maier, On the mechanical behaviour of titanium alloy TiAl6V4 manufactured by selective laser melting: Fatigue resistance and crack growth performance, Int. J. Fatigue. 48 (2013) 300–307. doi:10.1016/j.ijfatigue.2012.11.011.

[2] C. Yan, L. Hao, A. Hussein, S.L. Bubb, P. Young, D. Raymont, Evaluation of light-weight AlSi10Mg periodic cellular lattice structures fabricated via direct metal laser sintering, J. Mater. Process. Technol. 214 (2014) 856–864. doi:10.1016/j.jmatprotec.2013.12.004.

[3] H. Brodin, J. Saarimäki, Mechanical properties of lattice truss structures made of a selective laser melted superalloy, 13th Int. Conf. Fract. (2013) 1–10. doi:10.1115/GT2013-95878.

[4] Y.M. Wang, T. Voisin, J.T. McKeown, J. Ye, N.P. Calta, Z. Li, Z. Zeng, Y. Zhang, W. Chen, T.T. Roehling, R.T. Ott, M.K. Santala, P.J. Depond, M.J. Matthews, A. V. Hamza, T. Zhu, Additively manufactured hierarchical stainless steels with high strength and ductility, Nat. Mater. 17 (2017). doi:10.1038/nmat5021.

[5] M. Shiomi, K. Osakada, K. Nakamura, T. Yamashita, F. Abe, Residual Stress within Metallic Model Made by Selective Laser Melting Process, CIRP Ann. - Manuf. Technol. 53 (2004) 195–198. doi:10.1016/S0007-8506(07)60677-5.

[6] V. Cain, L. Thijs, J. Van Humbeeck, B. Van Hooreweder, R. Knutsen, Crack propagation and fracture toughness of Ti6Al4V alloy produced by selective laser melting, Addit. Manuf. 5 (2015) 68–76. doi:10.1016/j.addma.2014.12.006.

[7] M. Smith, Z. Guan, W.J. Cantwell, Finite element modelling of the compressive response of lattice structures manufactured using the selective laser melting technique, Int. J. Mech. Sci. 67 (2013) 28–41. doi:10.1016/j.ijmecsci.2012.12.004.

[8] ASTM International, Standard Specification for Additive Manufacturing Titanium-6 Aluminum-4 Vanadium with Powder Bed Fusion, i (2012) 1–8. doi:10.1520/F2924-12A.2.

[9] S.K. Moon, Y.E. Tan, J. Hwang, Y.J. Yoon, Application of 3D printing technology for designing light-weight unmanned aerial vehicle wing structures, Int. J. Precis. Eng. Manuf. - Green Technol. 1 (2014) 223–228.

doi:10.1007/s40684-014-0028-x.

[10] T.A. Schaedler, W.B. Carter, Architected Cellular Materials, Annu. Rev. Mater. Res. 46 (2016) 187–210. doi:10.1146/annurev-matsci-070115-031624.

[11] M. Dumas, P. Terriault, V. Brailovski, Modelling and characterization of a porosity graded lattice structure for additively manufactured biomaterials, Mater. Des. 121 (2017) 383–392. doi:10.1016/j.matdes.2017.02.021.

[12] S.L. Sing, W.Y. Yeong, F.E. Wiria, B.Y. Tay, Characterization of Titanium Lattice Structures Fabricated by Selective Laser Melting Using an Adapted Compressive Test Method, Exp. Mech. 56 (2016) 735–748. doi:10.1007/s11340-015-0117-y.

[13] S.L. Campanelli, N. Contuzzi, A.D. Ludovico, F. Caiazzo, F. Cardaropoli, V. Sergi, Manufacturing and characterization of Ti6Al4V lattice components manufactured by selective laser melting, Materials (Basel). 7 (2014) 4803–4822. doi:10.3390/ma7064803.

[14] B. Gorny, T. Niendorf, J. Lackmann, M. Thoene, T. Troester, H.J. Maier, In situ characterization of the deformation and failure behavior of non-stochastic porous structures processed by selective laser melting, Mater. Sci. Eng. A. 528 (2011) 7962–7967. doi:10.1016/j.msea.2011.07.026.

[15] T. Tancogne-Dejean, A.B. Spierings, D. Mohr, Additively-manufactured metallic micro-lattice materials for high specific energy absorption under static and dynamic loading, Acta Mater. 116 (2016) 14–28. doi:10.1016/j.actamat.2016.05.054.

[16] J.A. Harris, R.E. Winter, G.J. McShane, Impact response of additively manufactured metallic hybrid lattice materials, Int. J. Impact Eng. 104 (2017) 177–191. doi:10.1016/j.ijimpeng.2017.02.007.

[17] L. Xiao, W. Song, Additively-manufactured functionally graded Ti-6Al-4V lattice structures with high strength under static and dynamic loading: Experiments, Int. J. Impact Eng. 111 (2017) 937–948. doi:10.1016/j.ijimpeng.2017.09.018.

[18] K.T. Ramesh, High Strain R 33.1, Handb. Exp. Solid Mech. (2008) 874.

[19] B. Vrancken, L. Thijs, J.-P. Kruth, J. Van Humbeeck, Heat treatment of Ti6Al4V produced by Selective Laser Melting: Microstructure and mechanical properties, J. Alloys Compd. 541 (2012) 177–185.

doi:10.1016/j.jallcom.2012.07.022.

[20] ASTM Standard E9-09, Standard Test Methods of Compression Testing of Metallic Materials at Room Temperature, Annu. B. ASTM Stand. 3.01 (2012) 92–100. doi:10.1520/E0009-09.2.

[21] R. Fadida, D. Rittel, A. Shirizly, Dynamic Mechanical Behavior of Additively Manufactured Ti6Al4V With Controlled Voids, J. Appl. Mech. 82 (2015) 41004. doi:10.1115/1.4029745.

[22] H. Kolsky, An Investigation of the mechanical properties of materials at very high rates of Loading, 676 (1949).

[23] J. Liu, S. Pattofatto, D. Fang, F. Lu, H. Zhao, Impact strength enhancement of aluminum tetrahedral lattice truss core structures, Int. J. Impact Eng. 79 (2015) 3–13. doi:10.1016/j.ijimpeng.2014.06.013.

[24] Ansys Inc, Explicit Dynamics Analysis Guide, Online. (n.d.). https://www.sharcnet.ca/Software/Ansys/17.0/en-us/help/exd_ag/exd_ag.html.

[25] Z. Ozdemir, E. Hernandez-Nava, A. Tyas, J.A. Warren, S.D. Fay, R. Goodall, I. Todd, H. Askes, Energy absorption in lattice structures in dynamics: Experiments, Int. J. Impact Eng. 89 (2016) 49–61. doi:10.1016/j.ijimpeng.2015.10.007.

[26] I. Maskery, N.T. Aboulkhair, A.O. Aremu, C.J. Tuck, I.A. Ashcroft, Compressive failure modes and energy absorption in additively manufactured double gyroid lattices, Addit. Manuf. 16 (2017) 24–29. doi:10.1016/j.addma.2017.04.003.

[27] D. Karagiozova, M. Alves, N. Jones, Inertia effects in axisymmetrically deformed cylindrical shells under axial impact, Int. J. Impact Eng. 24 (2000) 1083–1115. doi:10.1016/S0734-743X(00)00028-2.

Appendix A

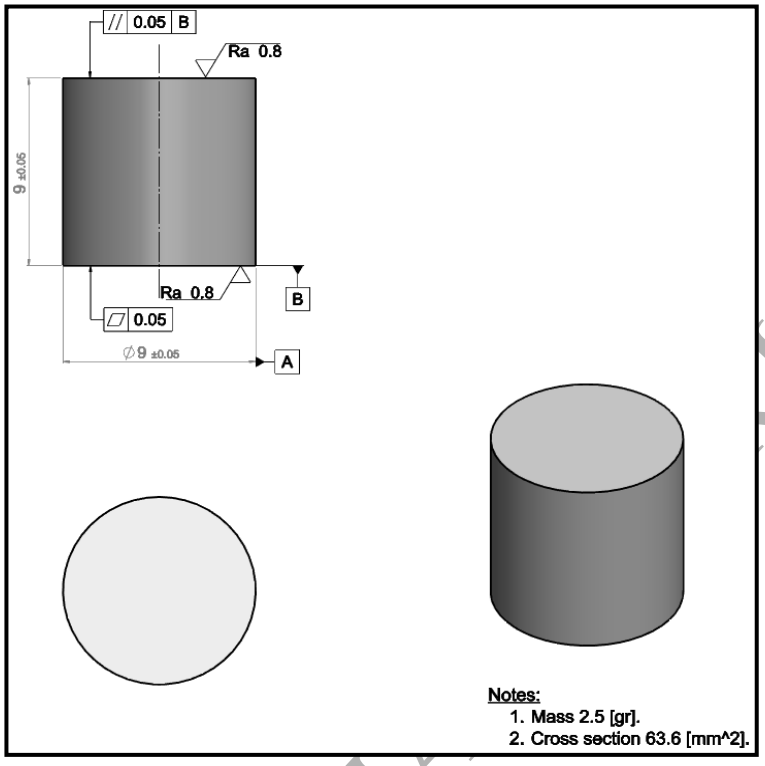

Fig. A1. Bulk specimen dimensions

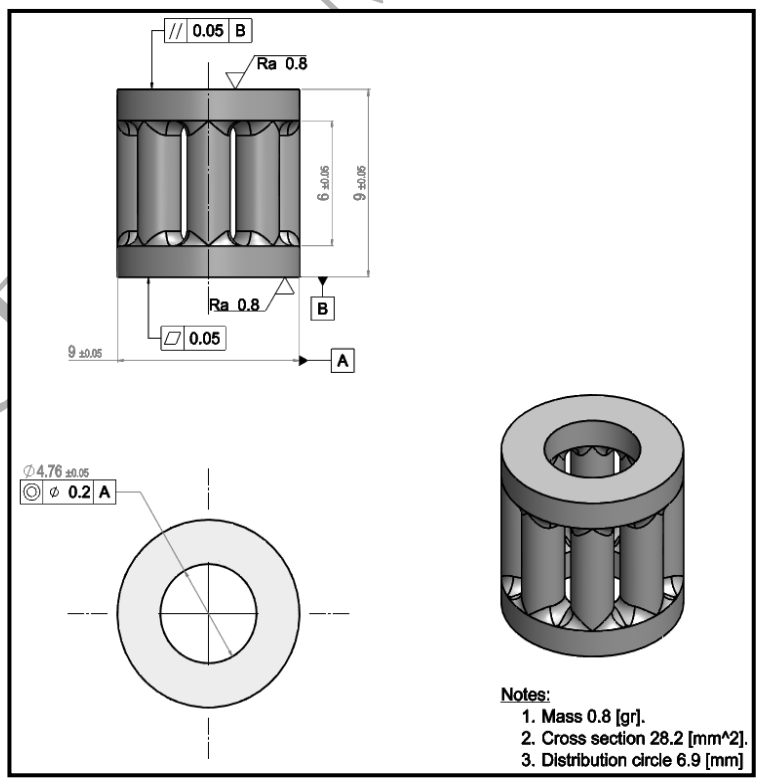

Fig. A2. 8-Column specimen dimensions

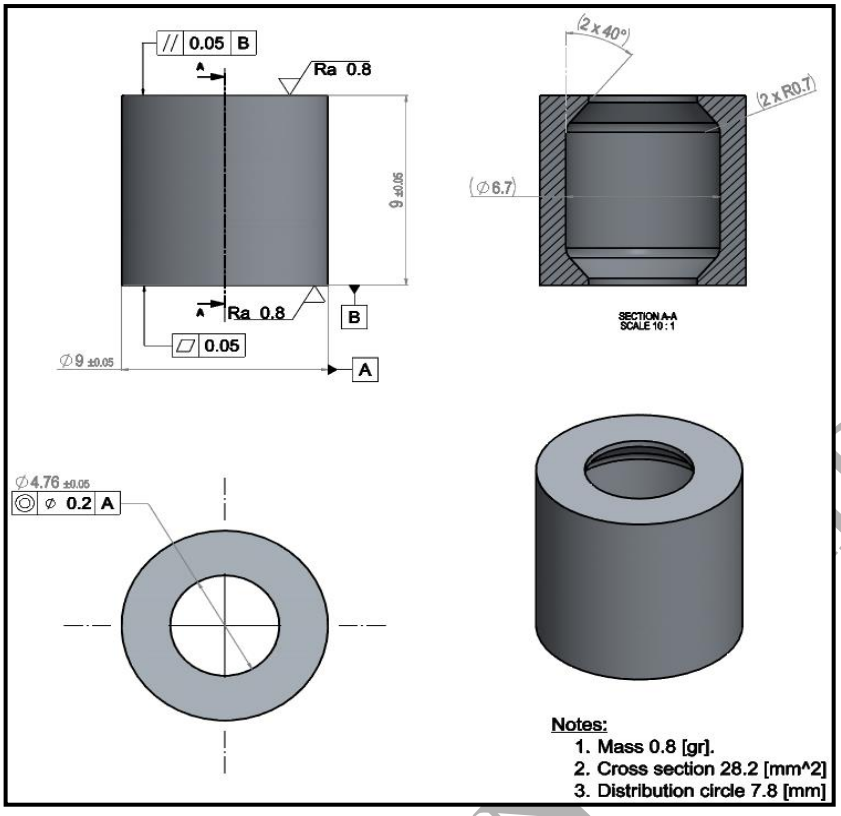

Fig. A3. Tube I specimen dimensions

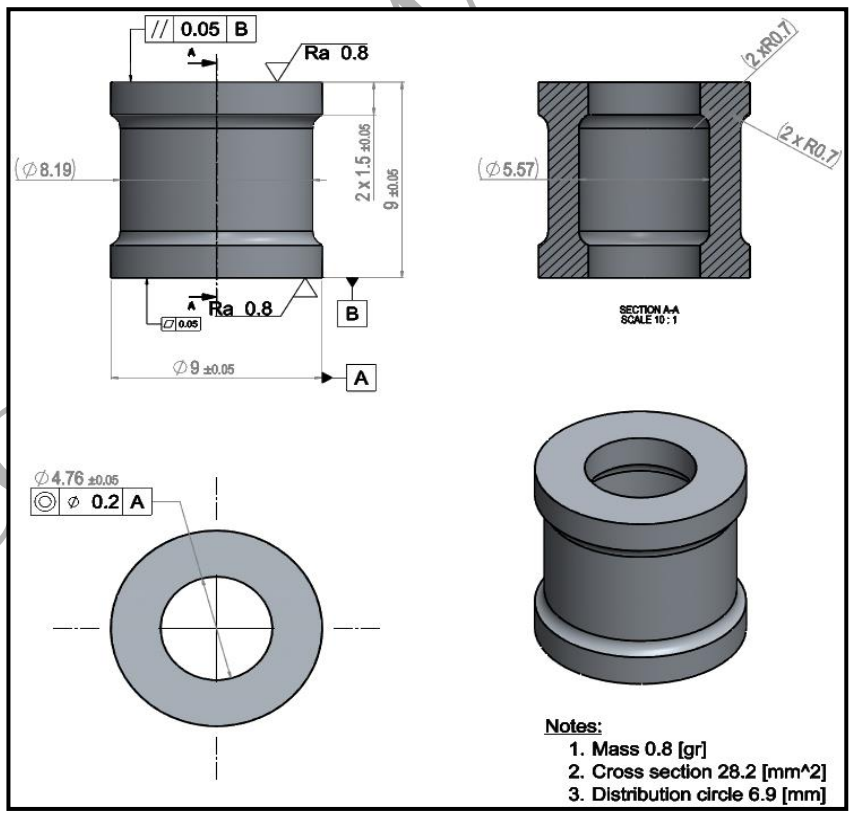

Fig. A4. Tube II specimen dimensions